LITHOS 440–441 (2023) 107021

Contents lists available at ScienceDirect

LITHOS

journal homepage: www.elsevier.com/locate/lithos

Mineralogy, geochronology, and geochemistry of the calc-alkaline Um Takha white granite pluton, South Sinai, Egypt

Madiha S.M. Osman [a], Mokhles K. Azer [b,*], Paul D. Asimow [c], Jason B. Price [c,d], Mauricio Ibañez-Mejia [e]

[a] Geology Department, Faculty of Science, Elmergib University, Libya
[b] Geological Sciences Department, National Research Centre, 12622-Dokki, Cairo, Egypt
[c] Division of Geological & Planetary Sciences, California Institute of Technology, Pasadena, CA 91125, USA
[d] Ibex Exploration LLC, Lakewood, CO 80228, USA
[e] Department of Geosciences, University of Arizona, AZ 85721, USA

ARTICLE INFO

Keywords:
Arabian-Nubian Shield
Sinai
Calc-alkaline granite
Zircon U-Pb dating
Zircon Hf isotopes
Cumulate
Post-collisional magmatism

ABSTRACT

The Um Takha white granite pluton (UTP) is exposed in west central Sinai (Egypt), in the northernmost segment of the Neoproterozoic Arabian-Nubian Shield (ANS). It is a member of the youngest suite of calc-alkaline granites in south Sinai. The UTP intrudes metamorphosed country rocks and diorites and is in turn intruded by the Serbal alkaline granite pluton. The UTP comprises a single phase of leucocratic monzogranite that contains alkali feldspar, plagioclase, quartz, biotite, and rare muscovite. U-Pb ion probe zircon dating for two samples of the white granite yields ages of 614.9 ± 6.3 and 581.5 ± 10.9 Ma, but the younger sample reveals abundant evidence that its zircons were affected by late corrosive fluids (e.g., discordance and patchy cathodoluminescence zoning); the 614.9 ± 6.3 Ma age is preferred. Geochemically, the UTP displays a limited compositional range (SiO_2 = 72.9–75.1 wt%) of mostly high-K calc-alkaline rocks of metaluminous to weakly peraluminous character, typical of the calc-alkaline granitoids of the early post-collisional stage of the northern ANS. The variation diagrams and parallel rare-earth element (REE) patterns for the white granite samples (n = 22) suggest that they represent one cogenetic suite. The UTP was likely generated by partial melting of a Na-rich amphibole-bearing tonalite source from the juvenile crust. This is consistent with the Hf isotope ratios of zircons from the UTP, which consistently yield positive $\varepsilon_{Hf}(t)$ values. The proposed trigger for the formation of the UTP is lithospheric delamination; its emplacement was associated with extensive denudation of the pre-630 Ma orogenic edifice as well as the 630–600 Ma post-collisional products, heat transfer into the lower crust, and post-collisional magmatism. Although the UTP is a cogenetic body, the traditional liquid-line-of-descent fractional crystallization approach fails to explain the large dynamic range of trace element contents over a limited range in major elements. We show that an alternative variable-proportion cumulate-liquid sampling interpretation of the whole-rock compositions, in which the most evolved sample represents a liquid composition and the least evolved sample is a low melt-fraction crystal mush, offers a physically reasonable scenario for the observed suite.

1. Introduction

Late Neoproterozoic basement rocks of the Sinai Peninsula lie at the extreme northern end of the Arabian-Nubian Shield (ANS). The ANS includes crystalline rocks of Neoproterozoic age and represents one of the largest juvenile blocks of continental crust on Earth (Ali et al., 2010; Johnson, 2003; Meert, 2003; Stoeser and Frost, 2006; Azer et al., 2017). The ANS was subjected to various episodes of deformation, metamorphism, and igneous activity that record subduction and accretion events associated with the closure of the Mozambique Ocean and the amalgamation of Western and Eastern Gondwana (Azer et al., 2019). The evolution of the ANS from ~1000 to 580 Ma can be divided into successive stages of island arc activity, collisional accretion, and finally post-collisional magmatism.

Post-collisional magmatism in the ANS resulted in the formation of voluminous high-K calc-alkaline and alkaline/peralkaline granitoids and their equivalent volcanic rocks (Azer et al., 2010; Azer and Asimow, 2021; Abuamarah et al., 2021a, b, 2022). Indeed, post-collisional

* Corresponding author.
E-mail addresses: mokhles72@yahoo.com, mk.abdel-malak@nrc.sci.eg (M.K. Azer).

https://doi.org/10.1016/j.lithos.2023.107021
Received 15 August 2022; Received in revised form 23 November 2022; Accepted 6 January 2023
Available online 13 January 2023

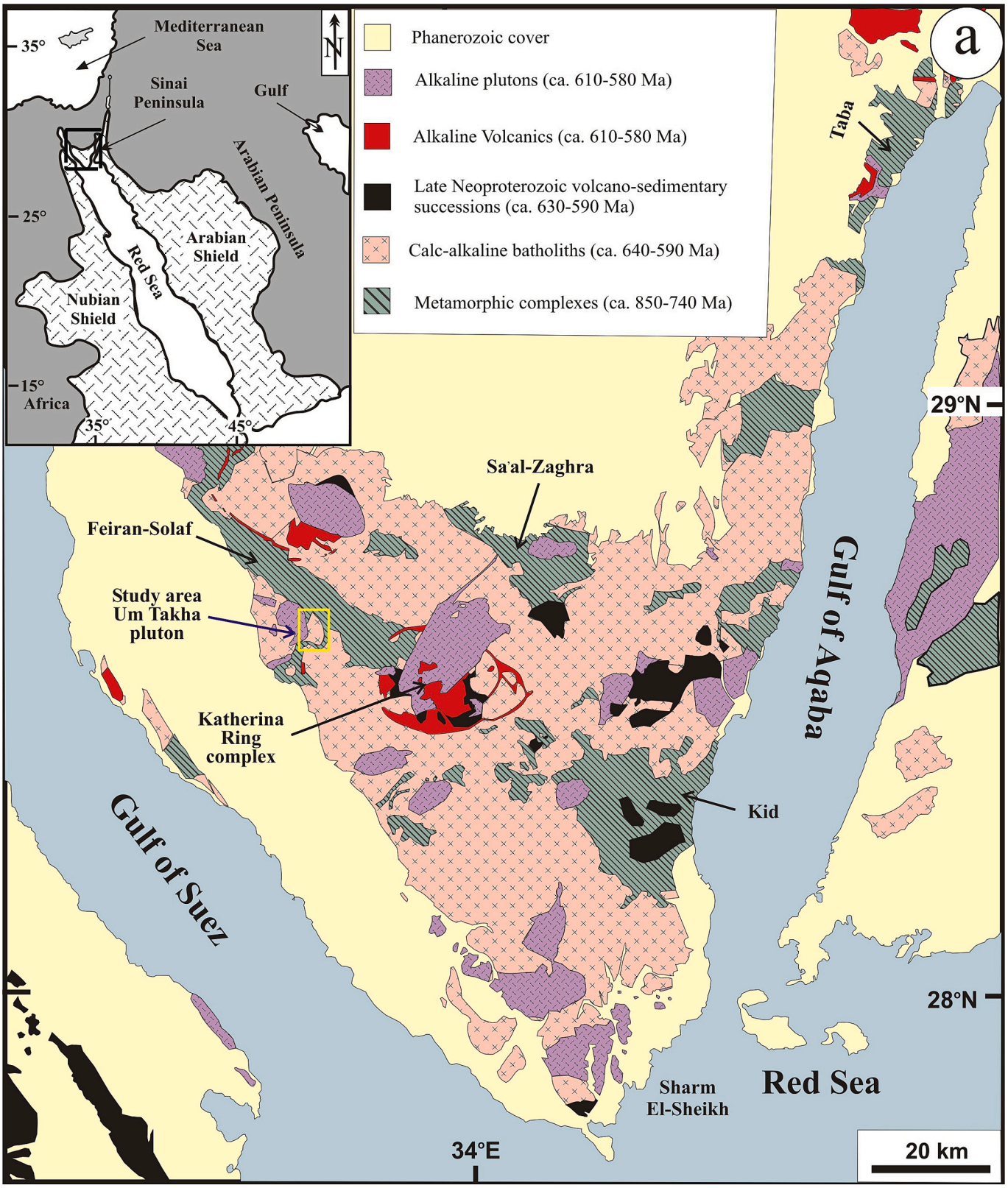

Fig. 1. (a) Geological map of Sinai Peninsula (modified after Be'eri-Shlevin et al., 2011) with inset index map of the Arabian-Nubian Shield. Location of the study area displayed in panels (b) and (c) is marked by a yellow rectangle. (b) Satellite image (from Google Earth™) of Wadi Um Takha area; the line of section in panel (d) is marked. (c) Geologic map of Wadi Um Takha area, modified after Eyal et al. (2015); sample locations are marked. (d) Schematic geological cross-section showing the inferred relationships between the Um Takha Pluton (UTP) and its country rocks. (For interpretation of the references to colour in this figure legend, the reader is referred to the web version of this article.)

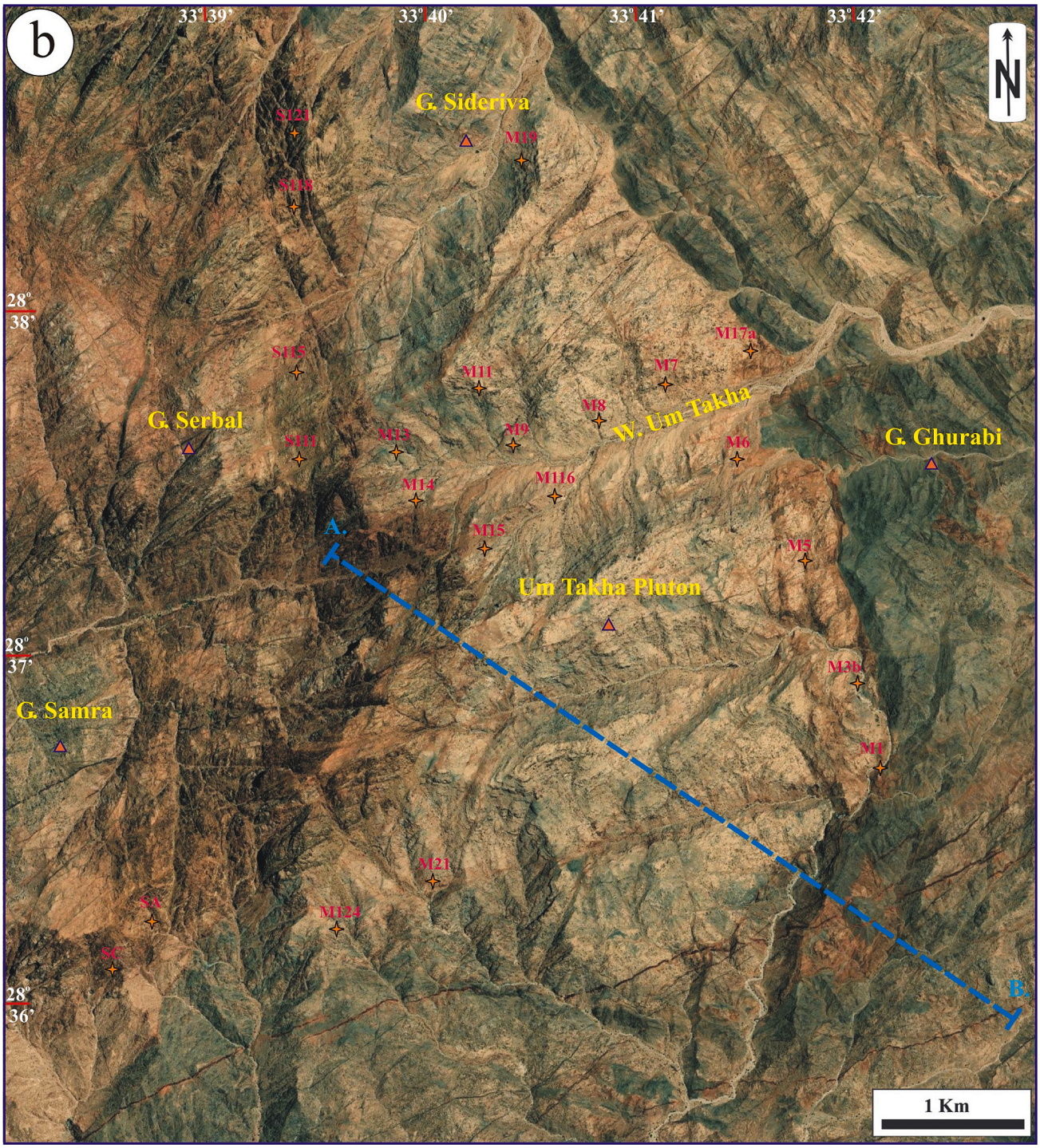

Fig. 1. (*continued*).

granites are one of the most important components of the juvenile upper crust of the Sinai Peninsula (Azer et al., 2014; Farahat and Azer, 2011; Gahlan et al., 2016; Khalil et al., 2018). These post-collisional granitoids can be divided into two major suites (Eyal et al., 2010; Be'eri-Shlevin et al., 2009a, b): high-K calc-alkaline granites and alkaline/peralkaline granites. Published ages for high-K calc-alkaline granites range from 620 to 597 Ma, whereas alkaline/peralkaline granites have yielded ages from 602 to 594 Ma (Be'eri-Shlevin et al., 2009a, b; Moreno et al., 2012). That is, there appears to have been an approximately five-million-year period during which both magma types were forming; refining the timing and duration of this overlap period is a high priority for further geochronological work in the area. In general, post-collisional granitoids in south Sinai are quite diverse in their texture, structure, mineralogy, and geochemistry; they encompass magmatic units ranging from small dikes to ring complexes to large batholiths. Published studies of this complex group of rocks contain several conflicting interpretations of their petrogenesis.

The only published study of the general geology of the Wadi Um Takha area is a structural study (El-Shafei and Kusky, 2003), with no information on the geochemistry or geochronology of the Um Takha white granite pluton (UTP). This contribution presents the first detailed study of the UTP, including field work, petrography, mineral chemistry,

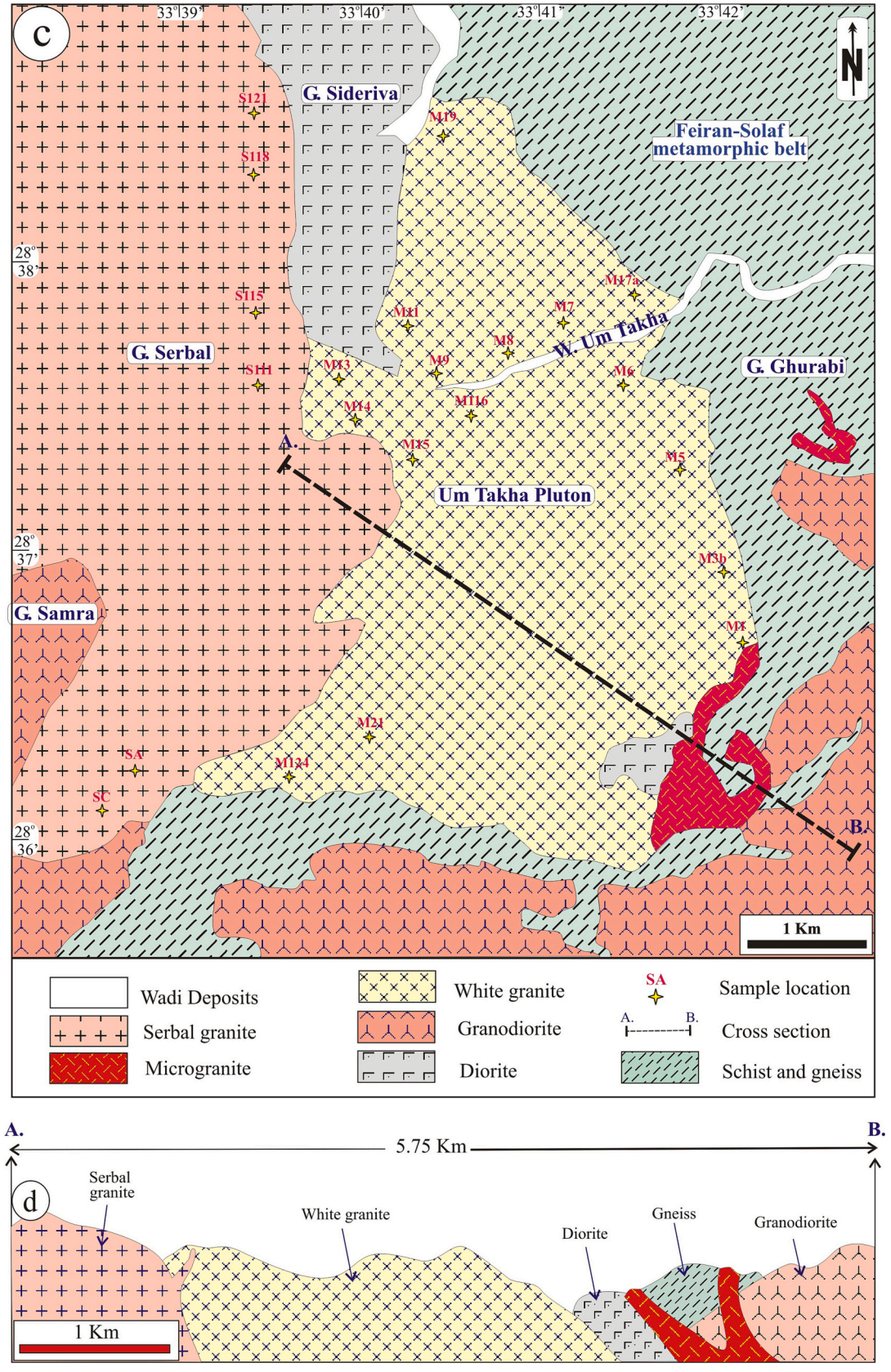

Fig. 1. (*continued*).

whole-rock chemistry, zircon U-Pb geochronology, and zircon Hf isotope ratios. The main goal of this work is to assess the timing of emplacement of calc-alkaline granite in the region, the role of intracrustal melting in its magmatic source, and to offer a novel framework for understanding the meaning of major and trace element variations within a granitoid pluton. These results in turn support a

discussion of the evolution of the juvenile crust of the ANS in the closing stages of the Pan-African orogeny.

2. Geological background

Our field, geochemical, and geochronological study of the UTP is aimed at placing this locality into the general scheme of evolution of the northern ANS through the Neoproterozoic. The UTP crops out in west central Sinai (Fig. 1a). It lies between 28°35′35″ & 28°38′55” N latitude and 33°38′05″ & 33°42′50″ E longitude and is readily evident both in the field and in satellite images by its strikingly light-colored exposures (Fig. 1b). The study area features exposures of late Neoproterozoic metamorphic and granitoid rocks (Fig. 1c), dissected by alluvium-filled wadi deposits. The relationships between the different parts of the UTP and country rocks are indicated schematically in a NW-SE cross-section, looking NE (Fig. 1d).

The metamorphic rocks, the oldest rock units in the mapped area, belong to the Feiran–Solaf metamorphic belt (Fig. 1a). This 35 km long, NW-striking belt (El-Shafei and Kusky, 2003; Azer et al., 2012) features several varieties of quartzofeldspathic and hornblende-biotite gneiss, migmatite, and calc-silicate schist. In the study area these schists and gneisses are crosscut by numerous unmetamorphosed dykes of various compositions.

A suite of diorite, granodiorite and lesser tonalite that intrudes the metamorphic units shows the characteristics of the subduction-phase *syn*-collisional granitoids (G1 of Hussein et al., 1982). Contacts between rock types in this general suite are gradational. They exhibit spheroidal weathering that results in gently sloping hills of low to moderate elevation. Diorite forms an undeformed elongated body at Gabal Sideriva containing xenoliths of darker diorite, gabbro, and amphibolite. The elongation of the intrusion suggests that it may have intruded along a pre-existing crustal weak zone between the Solaf and Feiran belts. The granodiorite and tonalite are gray, medium- to coarse-grained rocks, highly fractured and rich in mafic minerals. The distinctive feature of this granodiorite is the common presence of mafic microgranular enclaves and xenoliths. Dike swarms are a common feature of the *syn*-tectonic granitoids.

The post-collisional granites in the Wadi Um Takha area form large mountainous outcrops bordering both the metamorphic belt and the syntectonic granitoids. They include the calc-alkaline white granite of the UTP and the alkaline granite of the Serbal pluton as well as a few outcrops of microgranite (plausibly a quenched phase of the Serbal alkaline granite), all of which truncate the dike swarms found within the early syn-tectonic granitoids.

The UTP is an irregular elongated body trending N-S (Fig. 1b, c), about 7 km long and 1–4 km wide. It intruded the metamorphic rocks and diorite, with sharp intrusive contacts, and was in turn intruded by the alkaline granite of the Serbal pluton and by microgranite (Fig. 2a). The white granites form relatively high mountains with rounded or oval outlines. The highest peak of the Um Takha pluton rises to ~1600 m above sea level. The UTP is moderately jointed, dominated by a low-dip-angle joint set (Fig. 2b). Weathered surfaces of the white granite take on a yellowish tint. This granite is medium-grained and contains xenoliths of gneissose diorite (Fig. 2c). The dykes cutting through the metamorphic rocks and syntectonic granitoids are in turn truncated by the white granite. The Serbal pluton is considered, on the basis of one published date (Be'eri-Shlevin et al., 2011) and its alkaline affinity (Azer, 2013), to be a late Neoproterozoic (605–580 Ma) post-collisional A-type granite. It is characterized by discontinuous ring-shaped outcrops dislocated by later faulting (Azer, 2013). The alkaline granite of Gabal Serbal is devoid of mafic microgranular enclaves, mafic schlieren, or dikes.

3. Petrography

The texture and petrography of the post-collisional granites of the

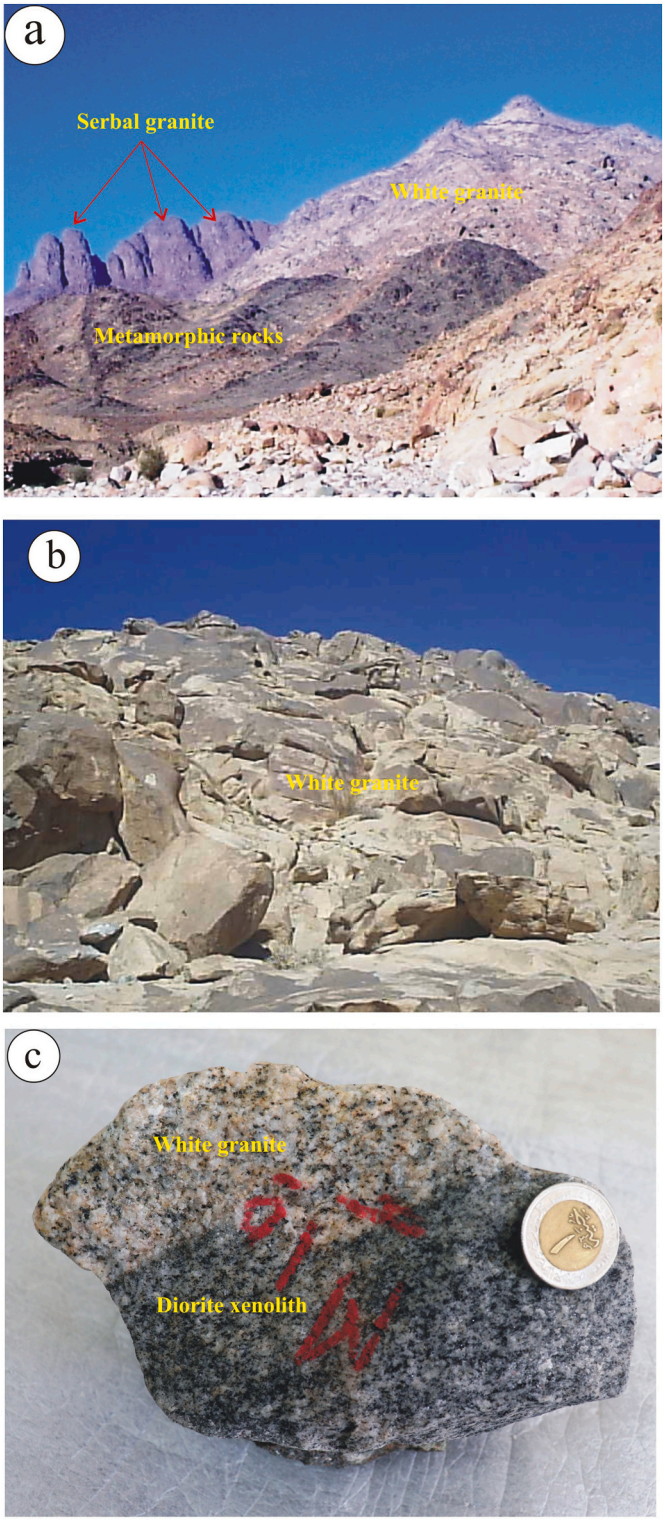

Fig. 2. Field photographs: (a) general view showing the UTP white granite intruded into metamorphic rocks and intruded by Serbal granite, (b) fractured and jointed white granite with yellowish weathering surfaces, and (c) xenolith of diorite gneiss within sharp contact against white granite.

Um Takha area (UTP white granite and Serbal alkaline granite) are described here to highlight the differences between them.

3.1. UTP white granite

Samples of white granite from the UTP are white on fresh surfaces and yellowish-white along fractures and weathered surfaces. These medium- to coarse-grained rocks display hypidiomorphic granular texture and uniform appearance throughout the pluton (Fig. 3a). Samples consist essentially of K-feldspar, plagioclase, quartz, biotite, and minor muscovite; the mineralogy is consistent with a monzogranite classification. Accessory minerals include zircon, allanite, apatite, and Fe-Ti oxides.

K-feldspar is the most common constituent and occurs as euhedral to subhedral tabular crystals including orthoclase, orthoclase-perthite, and microcline-perthite; the common perthitic texture is defined by fine linear exsolution lamellae (Fig. 4a). Intergrowths of quartz and K-feldspar in graphic and myrmekitic textures are also observed. Some orthoclase crystals have small quartz and biotite inclusions (Fig. 4b, c). Microcline shows very fine twinning, generally superimposed on perthitic exsolution to create complex extinction patterns in cross-polarized light. Microcline may have inclusions of biotite, quartz, and muscovite (Fig. 4d, e). Plagioclase occurs as euhedral to subhedral tabular crystals of albite and oligoclase. The original euhedral to subhedral outlines of tabular albite crystals are corroded by K-feldspar and quartz.

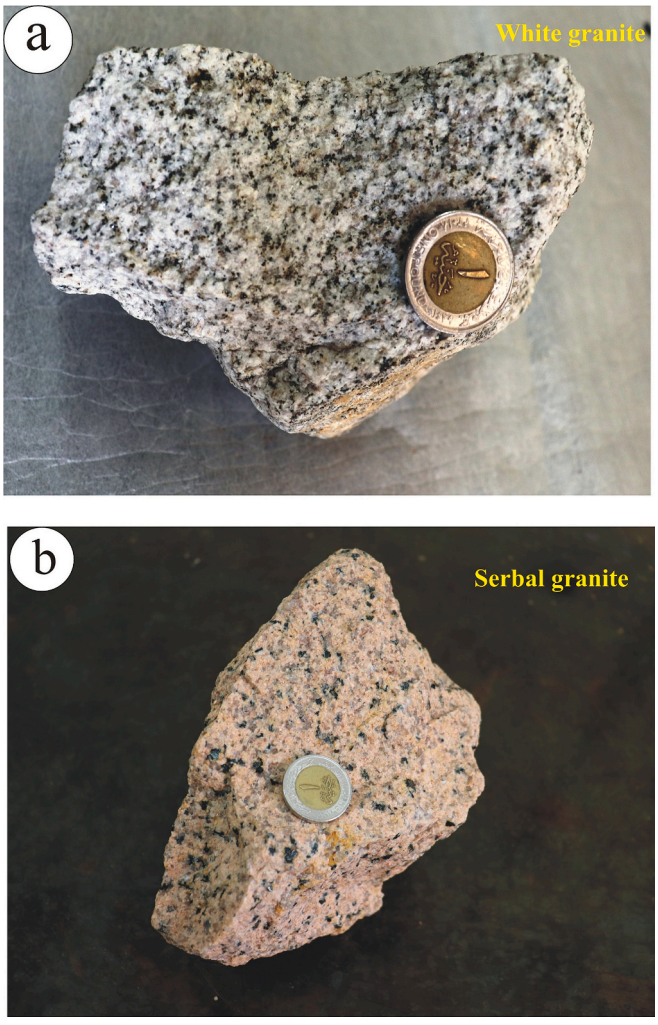

Fig. 3. Hand specimen photographs: (a) Sample of UTP white granite and (b) sample of Serbal alkaline granite.

Quartz occurs as subhedral to rounded anhedral grains filling interstices between feldspars or as fine aggregates and inclusions in K-feldspar. Both forms exhibit undulatory extinction and, locally, graphic intergrowths. Biotite is the most abundant mafic mineral; hornblende is comparatively scarce. Biotite occurs as small prismatic crystals or as fine interstitial flakes (Fig. 4f, h), variably altered to Fe-oxides, chlorite, and muscovite. The amphibole is strongly pleochroic and occurs as small anhedral crystals. Muscovite occurs as anhedral to subhedral flakes interstitial between K-feldspars and quartz and rarely as inclusions in them (Fig. 4g). Allanite occurs as anhedral crystals associated with biotite and partially replacing biotite along cleavage partings (Fig. 4h). Close to the Serbal granite, the proportion of secondary sodic-calcic alteration minerals increases; these include sericite (muscovite), quartz, albite, calcite, chlorite, and minor epidote.

3.2. Serbal granite

The Serbal granites are medium- to coarse-grained, equigranular, pink to pinkish-red rocks, dominantly alkali feldspar granite that grades into volumetrically less significant peralkaline granite (Fig. 3b). K-Feldspar and quartz are the main constituents with small amounts of albite and mafic minerals. The Serbal granite contains a wide range of accessory minerals such as apatite, zircon, Fe-Ti oxides, titanite, pyrochlore, fluorite, and allanite. Alkali feldspars are the most abundant constituents and are turbid with brown stains. Albite occurs as subhedral to anhedral prismatic crystals or as exsolved patches or stringers within K-feldspar host crystals. Quartz occurs mostly as coarse anhedral grains or as fine interstitial grains. The mafic minerals include biotite and amphibole. Biotite forms subhedral to euhedral crystals that contain zircon inclusions. Amphibole occurs as anhedral large crystals or as interstitial acicular crystals that are sodic-calcic or sodic in composition. Sodic amphibole is locally altered to Fe-rich biotite and opaque phases. Muscovite occurs in the interstices between other minerals or as fine inclusions in K-feldspar and quartz.

4. Analytical methods

Mineral chemical analyses were performed at the Department of Geosciences, University of Oslo, Norway, and at California Institute of Technology, USA (Caltech). The University of Oslo operates a CAMECA SX100 electron microprobe. Operating conditions were 15 kV, 15 nA, 2 μm diameter beam, counting time of 10 s on-peak and 5 s each at low and high background positions, natural and synthetic mineral standards, and a ZAF matrix correction routine. This instrument was used for carbon-coated thin sections of samples M15 and M21. At Caltech, chemical analyses and electron backscatter images of representative minerals in carbon-coated polished thick sections of samples M6 and M14 were acquired using the JEOL JXA-8200 electron probe at the Division of Geological and Planetary Sciences (GPS). Operating conditions were 15 kV, 25 nA, 1 μm beam, 20 s on-peak counting times, the mean atomic number background subtraction method, and the CITZAF matrix correction routine. The analytical standards used for analyses were synthetic forsterite, fayalite, Mn-olivine, anorthite, TiO_2, and Cr_2O_3; Amelia albite, Asbestos microcline, and Durango apatite.

Based on the petrographic studies, 22 rock samples (15 white granite, 6 alkaline granite and 1 microgranite) were analyzed for major, trace and rare earth elements at California Institute of Technology (Caltech, USA), GeoAnalytical Lab (Washington State University, USA) and Activation Laboratories Ltd. (Actlabs, Canada). At Washington State University, concentrations of major and trace elements were determined on fused beads with a ThermoARL X-ray fluorescence (XRF) Spectrometer. The analytical precision of these XRF analyses, as calculated from duplicate samples, is better than 1% (2σ) for most major elements and better than 5% (2σ) for most trace elements (errors are higher for Ni, Cr, Sc and V). Loss on ignition (LOI) is determined by weight difference after ignition at 1000 °C.

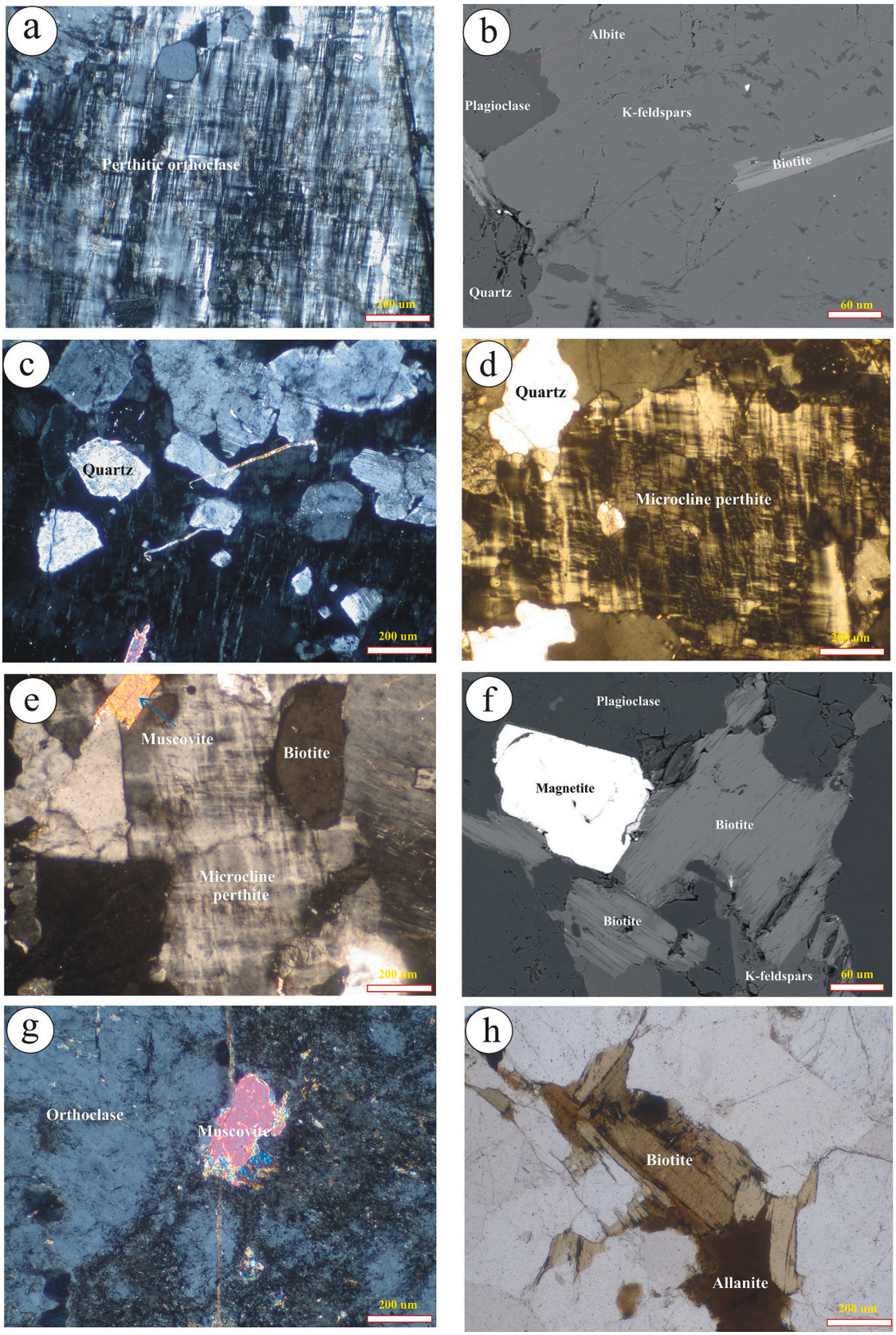

Fig. 4. Photomicrographs of UTP white granite in cross-polarized light (a, c, d, e and g), plane-polarized light (h) and electron backscatter images (b and f): (a) perthitic texture with fine and linear exsolution lamellae; (b) backscatter image showing biotite inclusion in K-feldspar; (c) many quartz inclusions in orthoclase; (d) microcline showing very fine cross-hatch twinning, perthitic exsolution, and small quartz inclusion; (e) microcline containing small biotite and muscovite inclusions; (f) backscatter image showing biotite corroded by feldspars; (g) anhedral muscovite crystal interstitial between feldspars; and (h) anhedral allanite associated with biotite.

At Caltech, rare earth elements (REE) and some trace elements in 12 samples were determined with an Agilent Technologies 8800 triple quadrupole ICP-MS. Coarsely crushed samples were milled to a fine powder in an agate ball mill. About 25 ± 1 mg of sample powder was dissolved in a new 50 mL polypropylene tube by refluxing in 2 mL of hot (100 °C) 3:1 nitric and hydrofluoric acid for at least 8 h, followed by dilution with milli-Q distilled water to 30 mL total volume. A working curve for instrument sensitivity was developed using USGS standards DTS-1, PCC-1, BCR-1, AGV-1, GSP-1, and G-2.

In the Actlabs analyses, rare earth elements and some trace elements for 4 samples were measured by ICP-MS following lithium borate fusion and acid digestion. Precision and accuracy of 2 to 5% for REE were determined by analysis of international reference materials and replicate analyses. Full details are on the laboratory website (actlabs.com).

Single-zircon U/Pb ages were obtained with the Cameca IMS 1270 secondary ion mass spectrometer at the UCLA national ion probe facility. Hand-samples weighing approximately 1 kg were crushed with a steel jaw crusher and rotating steel disk mill until all material passed through a 250 μm mesh sieve. The resulting powder was winnowed by hand in a water-filled gold pan. The heavy fraction was treated with a hand magnet, passed through a Frantz magnetic separator at currents of 0.4, 1.0, and 1.5 A, and then separated using Methylene Iodide heavy liquid (density 3.32 g/cm^3) to obtain a nearly pure zircon separate. Up to 10 grains of each sample were hand-picked for clarity and size under a binocular microscope and mounted in a 1″ circular epoxy disk along with grains of accepted international zircon age standards (FC1, Paces and Miller, 1993; AS3, Schmitz et al., 2003; Plešovice, Frei and Gerdes, 2009; and R33, Black et al., 2004). The mount was ground to expose zircon interiors and then polished with Al_2O_3 sandpapers and finally 0.25 μm diamond powder on a felt cloth in water.

The polished mount was carbon-coated and imaged in both backscattered electrons and cathodoluminescence (CL) on the Zeiss 1500VP field-emission SEM in the Caltech GPS analytical facility. The carbon coat was removed by repolishing with 1200 grit SiC sandpaper and cleaned by ultrasonicating in 5 M HCl for 30 min. A 30 nm Au coat was then applied and the samples were transferred to the analysis chamber of the ion probe. SEM imaging was repeated after analysis to verify spot positioning within grain interiors.

All data were collected in a single two-day session, 16 to 17 August 2016, on the UCLA IMS 1270. The instrument was operated with a 12.5 kV beam of primary $^{16}O^-$ ions at a current of 17.7 nA, yielding a 30 μm spot size. At a mass resolving power of 4800, the secondary ion beam was centered in the field aperture by using the HfO signal, which ranged between 150,000 and 200,000 counts per second. After a 20 s presputter, an automated mass calibration and peak centering routine was applied at each analytical spot, measuring in sequence a cycle of mass 203.5 (background), $^{94}Zr_2O$ (reference mass for all Pb isotopes, 1 s), ^{204}Pb (4 s), ^{206}Pb (6 s), ^{207}Pb (6 s), ^{208}Pb (2 s), ^{232}Th (2 s), ^{238}U (2 s), and $^{238}U^{16}O$ (1 s). Each analytical spot was collected by averaging 10 cycles through the mass range. ^{204}Pb was measured to enable a common Pb correction, but none of the analyzed zircons displayed ^{204}Pb counts above the background so the common Pb correction was not significant for any of the analyses. The relative sensitivity factors for Pb and U were obtained by using FC1 zircon as a primary standard and fixing its age at 1099.1 Ma. Repeat analyses of FC1 displayed an excellent linear correlation between UO/U and $^{206}Pb/U$ that was then used as a working curve for all other zircons on the same mount. Data were reduced using ZIPS 3.0.4 software (in-house UCLA software developed by C. Coath), which provides analytical uncertainties accounting for counting statistics in both the standard calibration and the unknown analysis. For each sample, a weighted mean age is computed by weighting the individual spot ages by their statistical variance. Uncertainty is reported as one standard error of the weighted mean, computed using Cochran's (1977) formula. The MSWD of the population is also reported; these are generally much less than unity, because the spot uncertainties contain both random and systematic error terms. Kernel density estimate plots for $^{238}U/^{206}Pb$ ages of standards are shown in Supplementary Fig. 1.

Although the ^{238}U-^{206}Pb, ^{235}U-^{207}Pb and ^{232}Th-^{208}Pb parent daughter pairs were analyzed, we report only $^{206}Pb/^{238}U$ ages in this work. $^{232}Th^{16}O$ was not analyzed, so the relative sensitivity factor correlation based on UO/U could not be applied to obtaining the $^{208}Pb/^{232}Th$ ratio. Furthermore, ^{207}Pb seems to have been affected by variable amounts of contamination. Initial analyses of an improperly cleaned mount showed extremely large ^{207}Pb excesses, up to a factor of two. After subsequent re-polishing, cleaning, and re-coating, this problem became much smaller but it was still measurably present as discordance in FC1 standard zircon, which is known to be concordant. Although a correction was applied to force the average analysis of FC1 standard to be concordant, the majority of unknown grains showed slight discordance that we interpret not as Pb loss but as persistent errors in ^{207}Pb counting. The result is that $^{207}Pb/^{235}U$ ages are too high and $^{207}Pb/^{206}Pb$ ages are much too high and scattered to be useful.

The same zircons analyzed for U-Pb geochronology were subsequently measured for Hf isotope ratios and Lu/Hf ratios in the Arizona LaserChron (ALC) facility at the University of Arizona, USA. Analytical protocols followed the methods described in detail by Ibañez-Mejia et al. (2014, 2015) so only a brief summary is presented here. Masses 171 through 180 were simultaneously monitored using Faraday collectors fitted with 3×10^{11} Ω amplifying resistors on a Nu plasma MC-ICP-MS, which was coupled to a Teledyne Photon Machines *Analyte G2* excimer laser ablation system. Mass-bias factors to correct for Hf fractionation (β_{Hf}) were calculated for each cycle by internally normalizing the measured $^{179}Hf/^{177}Hf$ values relative to a reference ratio of 0.7325 (Patchett and Tatsumoto, 1980), using an exponential fractionation law. Ytterbium mass fractionation was corrected using a $^{173}Yb/^{171}Yb$ value of 1.129197 (Vervoort et al., 2004) and a session-specific $^{176}Yb/^{173}Yb$ bias correction factor determined from measurement of natural and synthetic high-REE/Hf reference zircon (see Ibañez-Mejia et al. (2015) for details). After Yb-Lu interference correction, $^{176}Hf/^{177}Hf$ values were normalized to a Mud Tank zircon value of 0.282507 (Woodhead and Hergt, 2005); this reference material was analyzed twice every ~15 unknowns during our session and its $^{176}Hf/^{177}Hf$ reproducibility was ±0.000061 (2 standard deviations), or ± 2.2 ε_{Hf}. Additionally, reference zircons FC1 and R33 were analyzed alongside our samples to monitor the accuracy of Hf bias and Yb interference corrections. These crystals are particularly well suited for this purpose due to their much higher (Yb + Lu)/Hf ratios compared to most natural crystals and other zircon reference materials (Ibañez-Mejia et al., 2015). During the session in which the samples reported here were analyzed, we obtained weighted average values of 0.282170 ± 0.000034 (n = 6) and 0.282753 ± 0.000032 (n = 6) for FC1 and R33, respectively. These values are within uncertainty of the JMC-475–normalized $^{176}Hf/^{177}Hf$ solution-MC-ICP-MS reference values for FC1 (0.282179 ± 0.000012) and R33 (0.282751 ± 0.000005) (Eddy et al., 2017), demonstrating data accuracy during our analytical session.

Table 1
Summary of $^{206}Pb/^{238}U$ ages for analyzed zircons.

Sample Name	n	weighted mean 206Pb/238 U age (Ma)	standard error of weighted mean (Ma)	MSWD
FC1[a]	17	1096.5	5.6	0.41
Plešovice[b]	4	338.5	0.5	0.02
AS3[c]	2	1103.5	7.5	0.93
R33[d]	5	446.3	5.2	0.53
M7	3	614.9	6.3	0.46
M14	7	581.5	10.9	2.28

[a] Primary standard, accepted age is 1099.0 ± 0.6 Ma (Paces and Miller, 1993).
[b] Secondary standard, accepted age is 339 ± 10 Ma (Frei and Gerdes, 2009).
[c] Secondary standard, accepted age is 1099.1 ± 0.2 Ma (Schmitz et al., 2003).
[d] Secondary standard, accepted age is 419.26 ± 0.39 Ma (Black et al., 2004).

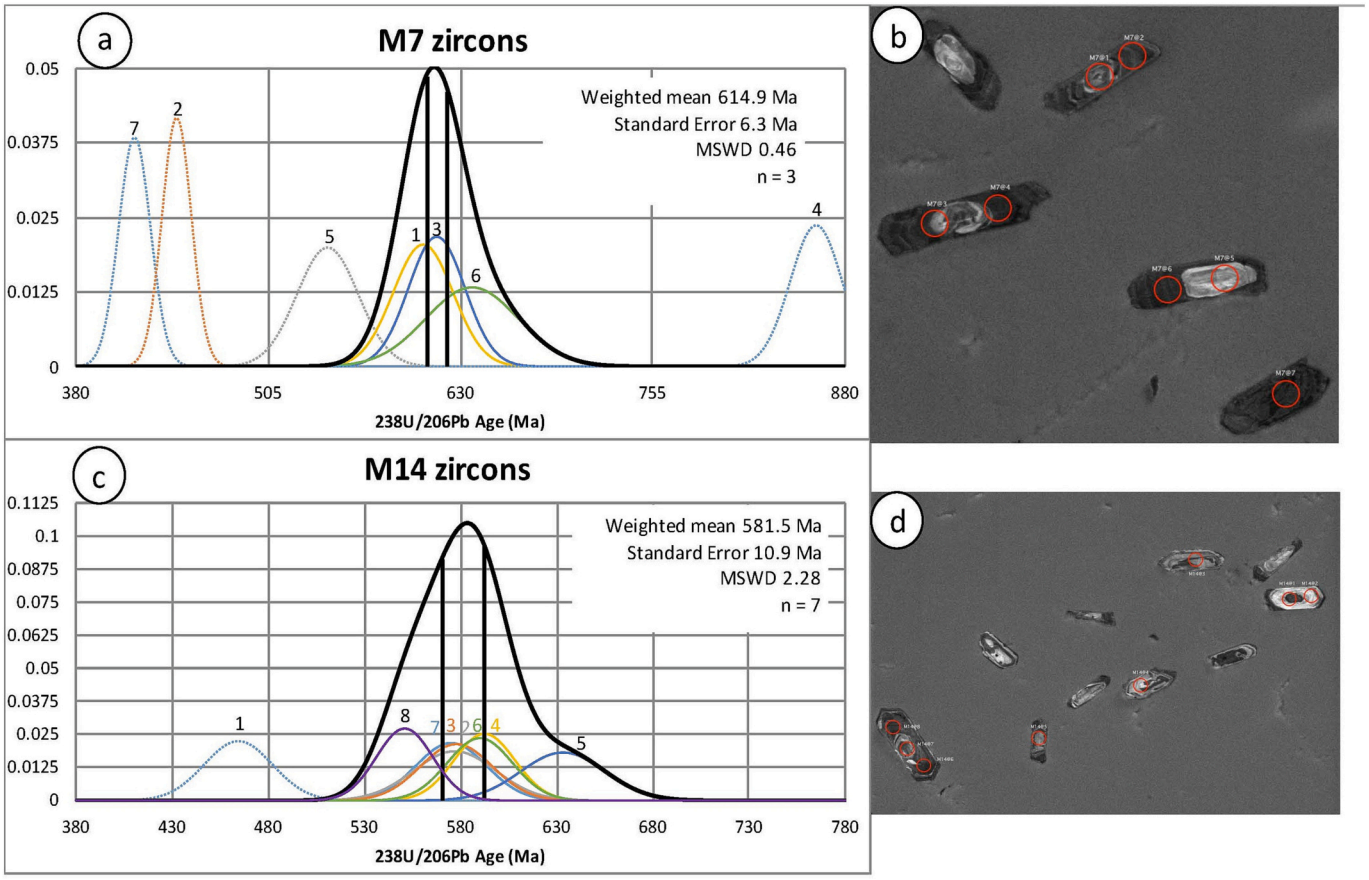

Fig. 5. Zircon U-Pb geochronology results. (a) Kernel density estimate (KDE) of $^{238}U/^{206}Pb$ age for zircons from sample M7. Each analysis spot is numbered; rejected spots are shown by dotted curves and accepted spots by solid curves. The sum of the solid curves is shown as a bold black probability curve, with one standard error above and below the mean indicated by vertical bars. (b) Cathodoluminescence (CL) image of the M7 zircons with numbered analysis spots marked by red circles 30 μm in diameter. (c) KDE plot for zircons from sample M14. (d) CL image of M14 zircons with analysis spots indicated. (For interpretation of the references to colour in this figure legend, the reader is referred to the web version of this article.)

5. Zircon results

5.1. Geochronology results

Results of ion probe U-Pb analysis are shown in Table 1 and Fig. 5. Zircons in both samples are sparse and small. Sample M7 yielded four usable zircons and sample M14 yielded five usable zircons, each a stubby prism about 50 × 100 μm. Most grains could only accommodate 1 or 2 ion probe spots. CL imaging indicates normal oscillatory growth zoning and a CL-bright core domain in most grains in M7. CL patterns in M14 are more complex, with some dark cores, patchy zoning patterns, and less visible oscillatory zones. The $^{238}U/^{206}Pb$ age for sample M7 is 614.9 ± 6.3 Ma (MSWD = 0.46, $n = 3$). Four outlier ages were rejected on the basis of being too young (418.2, 445.6, 543.7 Ma) or much too old (861.3 Ma); the rejected spots are also systematically more discordant than the accepted spots. The $^{238}U/^{206}Pb$ age for sample M14 is 581.5 ±

Table 2
Zircon Hf isotope results.

Sample	Spot number	$^{176}Hf/^{177}Hf(0)$	± 2 SE	$^{176}Lu/^{177}Hf$	$\varepsilon_{Hf}(0)$	± 2 SE	Spot Age	$\varepsilon_{Hf}(t)$	$\varepsilon_{Hf}(614.9)$	± 2 SE
M14	1	0.282610	0.000067	0.00338	−6.2	2.4	590.1	5.7	6.2	2.4
	2	0.282512	0.000079	0.00233	−9.7	2.8	575.2	2.3	3.2	2.8
	3	0.282620	0.000045	0.00363	−5.8	1.6	551	5.1	6.6	1.6
	4	0.282565	0.000097	0.00212	−7.8	3.4	592.5	4.6	5.1	3.4
	5	0.282617	0.000070	0.00187	−5.9	2.5	592.5	6.5	7.1	2.5
	6	0.282564	0.000080	0.00176	−7.8	2.8	592.5	4.7	5.2	2.8
	7	0.282520	0.000089	0.00165	−9.4	3.2	577	2.9	3.7	3.2
								weighted mean:	**5.5**	**1.4**
								MSWD:	**1.3**	
M7	1	0.282620	0.000045	0.00402	−5.8	1.6	614.6	6.2	6.3	1.6
	2	0.282620	0.000130	0.00400	−5.8	4.6	861.3	11.2	5.6	4.6
	3	0.282631	0.000087	0.00238	−5.4	3.1	614.6	7.3	7.3	3.1
	4	0.282672	0.000075	0.00554	−4.0	2.7	543.7	6.1	7.7	2.7
	5	0.282598	0.000085	0.00323	−6.6	3.0	418.2	1.8	6.2	3.0
	6	0.282686	0.000073	0.00250	−3.5	2.6	418.2	5.1	9.5	2.6
								weighted mean:	**7.1**	**1.4**
								MSWD:	**1.1**	

10.9 Ma (MSWD = 2.3, $n = 7$). One outlier age was rejected on the basis of being much too young (464.5 Ma). The scattered ages, high MSWD, irregular CL zoning patterns, and high discordance of the M14 data suggest that the age is unreliable. In combination with geologic context showing that the calc-alkaline UTP is intruded by the alkaline Serbal pluton with probable age 605 Ma, we find that the cluster of 3 most concordant zircons with normal igneous zoning patterns in sample M7 yields the most likely correct igneous age for the UTP. Hence, we report the age of the white granite as 614.9 ± 6.3 Ma.

5.2. Hf isotope results

We analyzed the same zircons studied by ion probe U-Pb using laser ablation for Hf isotopes and Lu/Hf ratios (Table 2). We placed laser spots directly on top of, or immediately adjacent to, each ion probe pit. The seven spots in sample M14 yield present day $\varepsilon_{Hf}(0)$ values ranging from −9.7 to −5.8, with a weighted average of −7.3 ± 1.6. There is no correlation between $\varepsilon_{Hf}(0)$ and the $^{238}U/^{206}Pb$ age of these spots so, given the high scatter in the individual U-Pb ages and the likelihood that all the zircons crystallized from the UTP magma at a common time (there are no inherited zircons in M14), we computed $\varepsilon_{Hf}(614.9\ Ma)$ for all seven spots. The results range from +3.2 to +7.1 and overlap within uncertainty, yielding a weighted average of +5.5 ± 1.4 (MSWD = 1.3). By contrast, using the individual spot ages to compute $\varepsilon_{Hf}(t)$ yields a range from +2.3 to +6.5 with a weighted average of +4.7 ± 1.5 and MSWD = 1.2. The results for the six spots in sample M7 are similar: present day $\varepsilon_{Hf}(0)$ values range from −6.6 to −3.5, with a weighted average of −5.2 ± 1.2. Again, $\varepsilon_{Hf}(0)$ and the $^{238}U/^{206}Pb$ age are uncorrelated. The computed $\varepsilon_{Hf}(614.9\ Ma)$ values overlap within uncertainty in the range from +5.6 to +9.5, yielding a weighted average of +7.1 ± 1.4 (MSWD = 1.1). By contrast, using the individual spot ages to compute $\varepsilon_{Hf}(t)$ yields a range from +1.8 to +11.2 with a weighted average of +6.0 ± 3.0 and MSWD = 2.8. In summary, both samples yield uniformly positive values of $\varepsilon_{Hf}(t)$.

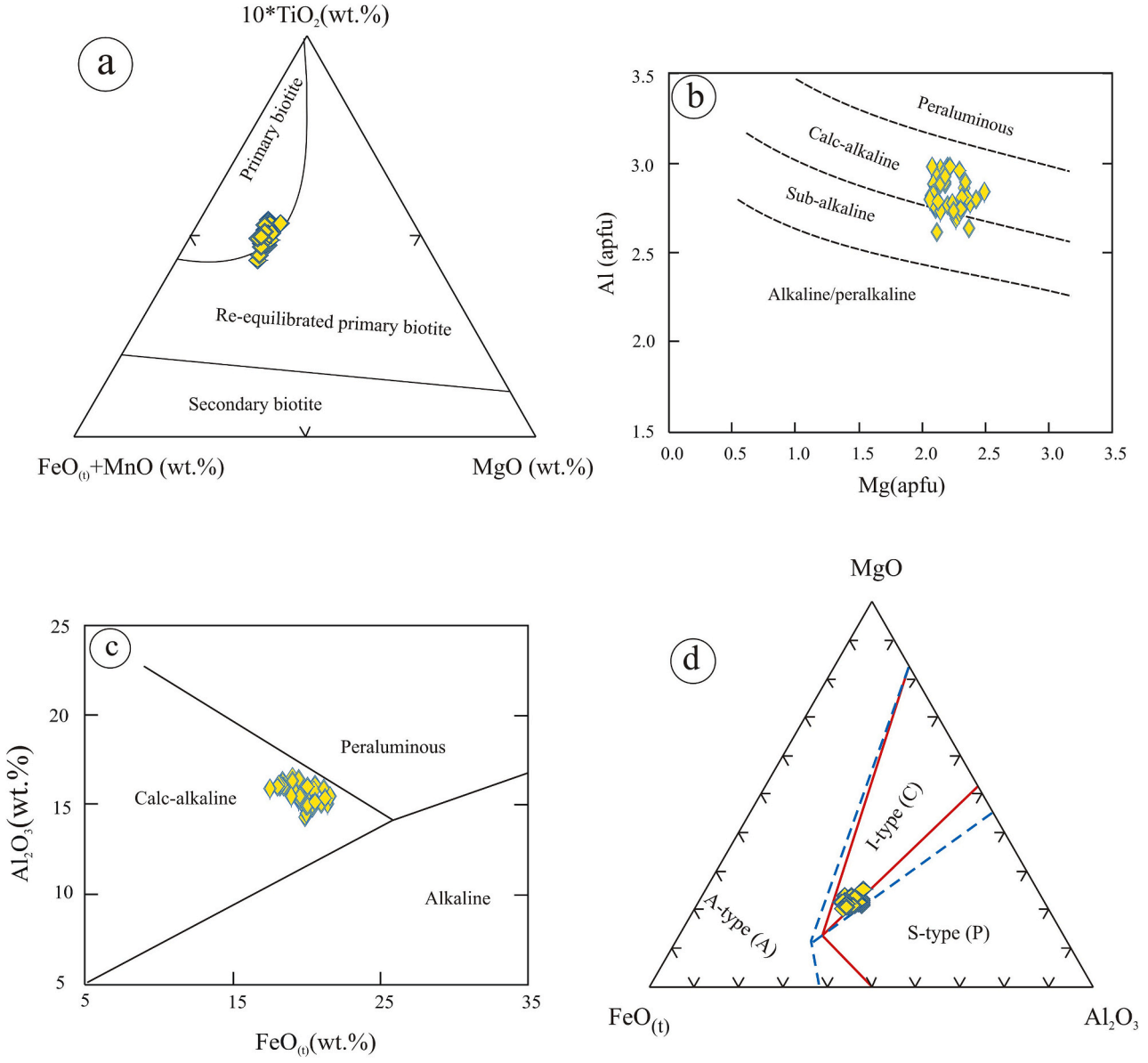

Fig. 6. Mineral chemistry of the white granite: (a) TiO_2-($FeO_{(t)}$ + MnO)-MgO ternary diagram for biotites (Nachit et al., 2005), (b) Al vs. Mg (atoms per formula unit, apfu) for biotites (Nachit, 1985); (c) $FeO_{(t)}$ vs. Al_2O_3 discrimination diagram for biotites (Abdel-Rahman, 1994), and (d) MgO-$FeO_{(t)}$-Al_2O_3 ternary diagram of biotite composition. Dashed lines are the original divisions determined by Abdel-Rahman (1994) for alkaline (A), calc-alkaline (C), and peraluminous (P) fields. Solid lines are new divisions proposed by Gion et al. (2022) to separate A-type, I-type, and S-type fields.

6. Mineral chemistry

Chemical compositions of the essential rock-forming minerals in the white granite of UTP were determined in four samples (M6, M14, M15 and M21) using electron microprobes at Caltech and the University of Oslo. The analyzed minerals include feldspars, biotite, and magnetite. All the microprobe data are given in the Supplementary Tables.

The chemical composition, structural formulae and end-member components of the analyzed feldspars are given in **Supplementary Tables 1S-3S**. According to the nomenclature of Deer et al. (1992), the feldspars are represented by orthoclase, albite, and oligoclase (note, this purely compositional classification does not distinguish true orthoclase from microcline). Orthoclase has Or contents ranging from 84.3 to 97.5 with an average of 93.2. The analyzed plagioclases include albite (An = 0.13–8.0; av. 1.90) and oligoclase (An = 10.1–23.2; av. 15.2). No attempt is made here to reconstruct the original compositions of exsolved perthites.

Biotite is the principal ferromagnesian mineral in the UTP white granite. Its chemical composition and structural formulae (on the basis of 22 oxygen atoms) are given in **Supplementary Table 4S**. The analyzed biotite crystals occupy a restricted range of composition. On the TiO_2-$FeO_{(t)}$-MgO ternary diagram of Nachit et al. (2005), all biotite analyses straddle the boundary between primary biotite and re-equilibrated primary biotite **(**Fig. 6a**)**. Using the biotite discrimination diagram of Nachit (1985), the biotite analyses plot mainly in the calc-alkaline field, with a few analyses extending into the sub-alkaline field **(**Fig. 6b**)**. On an Al_2O_3 vs. $FeO_{(t)}$ biotite discrimination diagram after Abdel-Rahman (1994), the biotite analyses plot in the calc-alkaline field **(**Fig. 6c**)**. On the MgO-$FeO_{(t)}$-Al_2O_3 ternary diagram of biotite composition after Gion et al. (2022), the analyzed biotites plot mainly in the field of I-type calc-alkaline granite **(**Fig. 6d**)**.

All the analyzed Fe-Ti oxides are classified as magnetite. Chemical composition and calculated structural formulae of magnetite are given in **Supplementary Table 5S**. The analyzed magnetite has a low TiO_2 concentration (<1.28 wt%), consistent with the Ti-poor appearance of the magnetite in reflected light. The ulvöspinel contents, calculated according to Störmer (1983), are below 0.05 mol%.

7. Geochemical characteristics

Previous studies of the Um Takha area have not reported any geochemical analysis of the UTP white granite. Whole-rock analyses, calculated normative mineral compositions, trace element concentrations, and REE contents of the white granite samples and some representative samples of the Serbal alkaline granites and microgranite are listed in Tables 3-5. The white granite is highly evolved, with SiO_2 concentrations ranging from 72.92 to 75.12 wt% and high differentiation index (DI = 90.58–94.14). On the R_1-R_2 diagram of De la Roche et al. (1980), the white granite samples plot in the granite field, whereas the Serbal alkaline granite samples plot in the alkali granite field (Fig. 7a). The microgranite sample plots on the boundary.

The white granite is medium- to high-K in composition (Fig. 7b) and shows characteristics of a "highly fractionated" calc-alkaline granite (Fig. 7c), though experimental evidence shows that similar rocks can be primary or nearly primary melts of intermediate crustal protoliths (e.g., Watkins et al., 2007). Serbal granite is highly fractionated alkaline granite, while microgranite is a typical alkaline rock (Fig. 7c). The alumina saturation index [ASI = molar ratio $Al_2O_3/(CaO + Na_2O + K_2O)$] in the UTP ranges between 0.97 and 1.03 (Table 1), reflecting metaluminous to slightly peraluminous character. The low agpaitic index of the UTP (AI ≤0.87; 0.79–0.86) indicates its calc-alkaline nature (Liégeois et al., 1998; Liégeois and Black, 1987), while Serbal granite and microgranite have high agpaitic index values (AI = 0.91–0.97), typical of alkaline rocks.

Variations in major oxide and trace element concentrations of the UTP white granite samples are illustrated in Figs. 8 and 9. The white granite samples of UTP show more or less coherent linear trends with no compositional gaps (Fig. 8). TiO_2, Fe_2O_3, MgO, CaO and Na_2O contents decrease with increasing SiO_2, whereas K_2O increases. Al_2O_3, MnO and P_2O_5 show no variation with increasing SiO_2. The concentrations of some trace elements show a decrease with increasing SiO_2 (Ba, Sr and Zr) whereas others systematically increase with increasing SiO_2 (Rb, Nb, Y, Ga, and Th, Fig. 9).

The primitive mantle-normalized multi-element diagram for the white granite and associated alkaline granites, using normalization values of Sun and McDonough (1989), is shown in Fig. 10a. It is clear that all the white granite samples show general similarities in their patterns. They are enriched in some LILE (Rb, K, Th) and HFSE (Ta, Zr, Nb, Hf), with negative troughs in P and Ti. The alkaline granitic rocks show completely different patterns than the white granite, most notably due to large negative anomalies of Sr and Ba.

Concentrations of REE together with notable ratios of normalized REE concentrations are given in Table 5 for the white granite and alkaline granite samples. Their chondrite-normalized REE patterns, using chondrite normalization values of Evensen et al. (1978), are given in Fig. 10b. The white granite is depleted in the REE (37–67 μg/g) compared to Serbal alkaline granite (161–200 μg/g) and microgranite (374 μg/g). The REE patterns of the white granite samples are subparallel; they all show enrichment in light REE relative to heavy REE [$(La/Lu)_n$ = 7.6–18.9]. Eu anomalies in the white granite samples are minor and vary from slightly negative to moderately positive [Eu/Eu* = 0.72–1.76]. Furthermore, the white granite shows a concave-up HREE pattern which may be the result of early amphibole fractionation or residual source amphibole (Be'eri-Shlevin et al., 2011; Sisson, 1994). The Serbal alkaline granite samples have much flatter overall REE patterns [$(La/Lu)_n$ = 2.9–4.1] and extreme negative Eu anomalies [Eu/Eu* = 0.03–0.04]. The microgranite is LREE-enriched [$(La/Lu)_n$ = 15.2] and has a moderate negative Eu anomaly [Eu/Eu* = 0.53].

8. Discussion

Post-collisional magmatism in the northernmost ANS commenced at ca. 635–625 Ma and culminated at 620–580 Ma, with a transition from batholithic calc-alkaline to alkaline A-type granite magmatism at ca. 605–600 Ma. In southern Sinai, post-collisional magmatism is widely distributed. Understanding the origin of post-collisional magmatism plays an important role in the stabilization of the ANS juvenile crust (Patchett and Chase, 2002; Stern et al., 2004). However, the origin of post-collisional magmatism is a general puzzle for plate-tectonic theory and controversy has surrounded the origin of post-collisional high-K calc-alkaline granitic magmas in southern Sinai (Azer, 2007; Azer and Farahat, 2011; Be'eri-Shlevin et al., 2009a; Eyal et al., 2010; Farahat and Azer, 2011; Khalil et al., 2018).

8.1. Tectonic setting

The latest known orogenic granites in the Sinai, with evidence of penetrative deformation and regional metamorphism, were dated at 635–640 Ma in the Kid metamorphic complex (Eyal et al., 2014), whereas emplacement of undeformed and unmetamorphosed K-rich calc-alkaline and alkaline granites followed over a protracted time span, 635–590 Ma (Be'eri-Shlevin et al., 2009b). Compositionally, the granitoid rocks exposed at Wadi Um Takha area are divided into three groups: (1) synorogenic calc-alkaline granitoids (the gneissose diorite unit), (2) late- to post-orogenic calc-alkaline granitoids (the undeformed UTP) and (3) post-orogenic alkaline rocks (the Serbal pluton and microgranite). The age of the white granite measured herein (615 ± 6 Ma) is similar to other highly evolved calc-alkaline plutons (ca. 605–600 Ma) in Sinai with similar geochemical traits (Be'eri-Shlevin et al., 2009b; Eyal et al., 2010).

A number of geochemical indicators confirm the calc-alkaline nature of the UTP and the alkaline nature of the Serbal pluton. Rb/Sr ratios of

Table 3
Major oxide contents and calculated normative compositions of white granite of UTP and associated alkaline granites.

Rock type	White granite of UTP															Serbal granite						Microgranite
Sample no.	M3b	M5	M6	M7	M8	M9	M11	M13	M14	M15	M16	M17A	M19	M21	M24	SC	SA	S111	S115	S118	S121	M1
Oxide wt%																						
SiO_2	75.12	74.88	74.51	73.12	73.44	73.66	73.13	73.46	73.76	72.97	72.92	73.29	74.21	74.08	73.95	77.15	77.56	77.9	77.36	78.24	76.68	70.01
TiO_2	0.04	0.05	0.06	0.1	0.11	0.08	0.12	0.08	0.12	0.14	0.16	0.09	0.05	0.07	0.05	0.06	0.09	0.06	0.05	0.06	0.19	0.42
Al_2O_3	13.41	13.48	13.26	13.73	13.52	13.48	13.47	13.43	14.49	13.62	14.03	13.37	13.53	13.43	13.47	11.66	12.27	11.75	11.44	11.76	12.09	14.34
Fe_2O_3	0.38	0.46	0.49	0.55	0.57	0.47	0.48	0.52	0.79	0.67	0.62	0.49	0.48	0.49	0.5	1.14	0.95	0.91	1.04	1.07	1.52	2.44
MnO	0.01	0.01	0.01	0.03	0.02	0.03	0.02	0.02	0.02	0.04	0.03	0.01	0.02	0.01	0.01	0.01	0.09	0.08	0.02	0.03	0.01	0.15
MgO	0.19	0.21	0.23	0.27	0.26	0.22	0.24	0.25	0.19	0.32	0.28	0.24	0.22	0.23	0.22	0.08	0.22	0.06	0.05	0.05	0.19	0.43
CaO	0.91	0.96	0.81	1.39	1.21	1.14	1.27	1.14	1.46	1.44	1.29	1.27	1.05	1.07	1.09	0.18	0.33	0.11	0.38	0.34	0.22	0.94
Na_2O	4.29	4.41	4.31	4.52	4.51	4.47	4.47	4.43	4.68	4.57	4.67	4.55	4.42	4.46	4.45	3.96	3.94	3.82	3.86	3.91	3.81	4.66
K_2O	4.11	4.01	3.97	3.58	3.38	3.36	3.42	3.59	3.42	3.25	3.35	3.72	3.79	3.8	3.55	4.39	4.55	4.39	4.24	4.23	4.36	4.95
P_2O_5	0.01	0.02	0.02	0.03	0.04	0.03	0.03	0.03	0.02	0.03	0.04	0.02	0.02	0.02	0.02	0.00	0.01	0.01	0.02	0.01	0.01	0.11
LOI	1.28	1.89	2.37	1.74	2.89	2.85	2.85	2.57	0.32	2.98	2.47	2.44	1.63	2.25	2.53	0.21	0.18	0.78	1.21	0.43	0.57	1.46
Total	99.75	100.42	100.04	99.06	99.95	99.79	99.5	99.52	98.96	100.03	99.86	99.49	99.42	99.91	99.84	98.63	100.19	99.87	99.67	100.13	99.65	99.91
Normative wt%																						
Quartz	32.55	31.83	32.76	30.43	32.12	32.91	31.94	31.97	30.06	31.12	30.44	30.5	31.94	31.54	32.51	36.73	35.71	38.43	37.98	38.09	36.77	20.92
Corundum	0.27	0.19	0.45	–	0.34	0.5	0.18	0.26	0.48	0.03	0.48	–	0.3	0.08	0.38	0.06	0.28	0.54	–	0.15	0.73	–
Orthoclase	24.67	24.07	24.03	21.75	20.59	20.49	20.92	21.89	20.44	19.8	20.34	22.66	22.91	23	21.57	26.33	26.9	26.2	25.47	25.09	26.04	29.77
Albite	36.87	37.9	37.35	39.32	39.33	39.03	39.15	38.68	40.04	39.86	40.59	39.68	38.26	38.66	38.71	34	33.36	32.64	33.2	33.21	32.58	40.13
Anorthite	4.52	4.7	3.98	6.77	5.92	5.63	6.32	5.63	7.19	7.16	6.31	5.21	5.2	5.3	5.42	0.91	1.57	0.49	1.38	1.63	1.04	3.64
Diopside	–	–	–	0.1	–	–	–	–	–	–	–	0.94	–	–	–	–	–	–	0.36	–	–	0.32
Hypersthene	0.91	1.04	1.12	1.2	1.22	1.06	1.03	1.19	1.28	1.47	1.24	0.63	1.11	1.1	1.13	1.57	1.71	1.32	1.22	1.42	2.07	3.46
Magnetite	0.1	0.12	0.12	0.15	0.16	0.13	0.14	0.14	0.21	0.19	0.18	0.13	0.12	0.13	0.13	0.27	0.25	0.23	0.25	0.25	0.38	0.67
Ilmenite	0.08	0.1	0.12	0.2	0.22	0.16	0.24	0.16	0.23	0.27	0.31	0.18	0.1	0.14	0.1	0.12	0.17	0.12	0.1	0.11	0.36	0.81
Apatite	0.02	0.04	0.04	0.07	0.09	0.07	0.07	0.07	0.04	0.07	0.09	0.05	0.04	0.04	0.04	–	0.02	0.02	0.04	0.02	0.02	0.24
Colour Index	1.08	1.25	1.36	1.64	1.59	1.35	1.41	1.49	1.72	1.94	1.73	1.87	1.33	1.36	1.35	1.96	2.13	1.67	1.92	1.79	2.81	5.26
Diff. Index	94.09	93.8	94.14	91.5	92.04	92.43	92.01	92.54	90.54	90.78	91.37	92.85	93.11	93.19	92.78	97.06	95.98	97.27	96.65	96.4	95.38	90.83
AI	0.86	0.86	0.86	0.82	0.82	0.82	0.82	0.83	0.79	0.81	0.81	0.86	0.84	0.85	0.83	0.97	0.93	0.94	0.96	0.94	0.91	0.91
ASI	1.02	1.01	1.03	0.99	1.02	1.03	1.01	1.01	1.03	1.00	1.03	0.97	1.02	1.00	1.02	1.00	1.02	1.05	0.98	1.01	1.06	0.97
R1	2507	2470	2489	2411	2481	2518	2468	2464	2425	2456	2395	2380	2473	2447	2500	2674	2676	2780	2762	2804	2691	1779
R2	370	378	358	431	408	397	412	398	450	437	427	410	389	389	392	252	287	245	268	270	270	403

Table 4
Trace element contents and ratios of white granite of UTP and associated alkaline granites.

Rock type	White granite of UTP															Serbal granite						Microgranite
Sample no.	M3b	M5	M6	M7	M8	M9	M11	M13	M14	M15	M16	M17A	M19	M21	M24	SC	SA	S111	S115	S118	S121	M1
(μg/g)																						
Ni	3.91	4.98	5.13	9.01	8.97	8.62	7.21	7.67	0.00	10.31	12.89	7.96	5.96	7.97	7.02	0.79	2.67	1.02	1.21	1.08	1.89	2.01
Cr	3.88	4.94	6.97	17.94	16.96	17.94	18.03	15.72	3.66	26.65	22.48	13.62	6.98	8.02	10.95	3.07	20.85	9.71	20.83	10.41	3.96	11.17
Co	1.99	2.52	2.04	4.97	4.57	4.18	3.78	4.96	–	5.04	5.71	3.95	2.07	2.96	2.99		5.55	2.11	3.76	4.21	2.84	9.08
Sc	4.13	5.96	9.52	20.93	17.03	12.94	12.92	11.02	0.69	25.93	20.93	14.83	7.97	9.96	12.04	0.40	8.43	4.97	5.55	10.24	3.21	13.84
V	0.86	0.92	1.42	3.02	3.21	2.87	3.12	2.26	16.34	3.72	4.01	2.83	1.28	1.55	2.14	2.97	3.62	0.86	0.99	1.12	0.95	13.12
Ba	543.06	556.92	637.07	828.12	744.69	650.97	667.17	625.62	828.53	664.53	715.74	643.99	574.39	664.85	607.21	147.41	97.76	29.25	40.48	54.74	111.46	855.63
Rb	119.14	123.85	119.43	114.46	118.12	117.12	115.64	114.12	73.46	108.94	112.36	116.86	124.52	119.63	118.17	139.39	146.26	174.02	225.37	222.68	170.01	123.92
Sr	346.75	444.06	440.27	653.15	665.22	619.27	576.32	559.99	601.03	698.89	702.68	615.96	527.29	452.23	542.47	29.50	108.33	14.62	15.47	16.86	25.27	113.62
Zr	88.42	100.69	100.43	131.1	124.3	120.55	115.76	115.57	68.10	123.06	128.41	114.37	106.03	105.69	111.41	198.10	199.79	223.57	234.4	248.44	252.72	528.52
Y	8.52	6.82	6.22	3.89	4.85	5.18	5.16	4.12	11.19	4.41	3.82	4.35	7.04	5.37	6.17	43.16	29.69	35.12	56.74	60.64	31.46	28.88
Nb	8.81	8.01	7.76	3.79	4.81	4.68	5.67	6.24	4.85	2.89	3.68	5.56	8.34	6.99	5.79	20.30	19.62	20.29	28.37	21.36	20.88	30.89
Ga	30.93	27.29	25.15	21.52	22.66	22.67	23.03	23.65	15.84	20.63	19.53	23.6	26.41	24.35	23.36	20.99	23.33	30.24	30.95	29.61	29.16	31.11
Cu	2.17	3.21	4.08	6.98	6.87	5.91	5.84	4.76	1.68	9.94	9.07	5.76	3.06	4.02	3.95	44.65	6.85	7.96	2.97	1.31	1.18	2.09
Zn	19.97	24.34	29.05	34.92	27.88	35.31	28.82	27.83	22.18	33.86	36.58	23.45	30.12	27.69	33.29	9.70	21.54	117.41	67.45	72.28	79.91	95.93
Pb	24.44	25.2	25.64	29.91	27.84	30.79	30.97	26.08	22.97	30.08	33.41	27.05	25.48	27.87	26.91	26.24	24.72	23.82	31.74	31.12	20.97	25.24
Th	7.02	5.98	3.96	1.78	2.13	2.34	2.98	2.96	4.06	1.11	1.02	2.74	4.98	3.22	3.98	17.03	10.32	20.49	22.81	23.92	16.98	20.19
U	2.04	2.09	1.63	0.96	0.82	0.98	0.99	1.07	0.40	0.94	0.74	1.05	1.46	1.54	1.25	5.74	7.64	5.97	11.94	9.33	2.2	3.02
Rb/Sr	0.34	0.28	0.27	0.18	0.18	0.19	0.20	0.20	0.12	0.16	0.16	0.19	0.24	0.26	0.22	4.72	1.35	11.90	14.57	13.21	6.73	1.09
Rb/Ba	0.22	0.22	0.19	0.14	0.16	0.18	0.17	0.18	0.09	0.16	0.16	0.18	0.22	0.18	0.19	0.95	1.50	5.95	5.57	4.07	1.53	0.14
K/Rb	34,118	33,288	32,956	29,719	28,058	27,892	28,390	29,802	28,430	26,979	27,809	30,881	31,462	31,545	29,470	36,447	37,771	36,443	35,198	35,114	36,194	41,091

Table 5
REE analyses of the white granite of UTP and associated alkaline granites.

Rock type	White granite of UTP									Serbal alkaine granite						Microgranite
Sample No.	M3b*	M6*	M7*	M9*	M11*	M13*	M14*	M15*	M17A*	S118*	SC*	S111	S115	SA	S121	M1*
(μg/g)																
La	9.091	11.830	8.452	9.878	10.475	14.691	11.420	13.858	8.921	23.362	25.427	28.254	26.79	27.262	24.937	86.615
Ce	17.871	21.763	15.571	19.682	20.190	29.012	22.719	27.190	17.799	60.452	59.668	70.508	66.757	69.904	65.012	166.437
Pr	2.154	2.488	1.738	2.335	2.311	3.361	2.669	3.309	2.069	8.427	8.088	10.054	9.255	10.075	9.387	18.040
Nd	8.292	9.148	6.428	9.059	8.761	12.885	10.315	12.943	7.980	35.529	31.839	45.531	39.529	43.705	39.572	68.299
Sm	1.857	1.888	1.242	1.932	1.912	2.466	2.131	2.526	1.653	9.853	8.093	11.576	10.23	10.757	10.298	10.285
Eu	0.398	0.531	0.626	0.424	0.477	0.517	0.569	0.508	0.537	0.080	0.094	0.101	0.086	0.092	0.087	1.552
Gd	1.347	1.372	0.949	1.387	1.368	1.750	1.590	1.817	1.227	7.950	6.478	10.124	8.844	9.289	7.522	7.699
Tb	0.216	0.213	0.125	0.195	0.192	0.229	0.218	0.242	0.175	1.474	1.208	1.59	1.501	1.609	1.326	1.108
Dy	1.150	1.068	0.595	0.907	0.879	0.994	1.001	1.053	0.836	8.184	7.081	9.807	8.603	8.975	7.775	5.654
Ho	0.237	0.206	0.113	0.164	0.153	0.168	0.181	0.186	0.155	1.681	1.534	1.922	1.762	1.798	1.629	1.151
Er	0.635	0.574	0.309	0.426	0.389	0.408	0.454	0.449	0.409	4.174	4.232	4.825	4.541	4.555	4.312	3.044
Tm	0.111	0.109	0.058	0.073	0.065	0.063	0.074	0.069	0.069	0.701	0.770	0.741	0.703	0.677	0.666	0.503
Yb	0.745	0.810	0.483	0.550	0.479	0.464	0.559	0.467	0.533	4.282	5.316	4.725	4.584	4.573	4.359	3.411
Lu	0.122	0.145	0.086	0.094	0.080	0.080	0.094	0.080	0.092	0.685	0.905	0.712	0.715	0.741	0.676	0.584
Eu/Eu*	0.77	1.01	1.76	0.79	0.90	0.76	0.95	0.72	1.15	0.03	0.04	0.03	0.03	0.03	0.03	0.53
$(La/Yb)_n$	8.25	9.88	11.84	12.14	14.80	21.43	13.82	20.05	11.32	3.69	3.23	4.04	3.95	4.03	3.87	17.17
$(La/Sm)_n$	3.09	3.96	4.29	3.23	3.46	3.76	3.38	3.46	3.41	1.50	1.98	1.54	1.65	1.60	1.53	5.32
$(Gd/Lu)_n$	1.35	1.16	1.35	1.81	2.09	2.69	2.07	2.80	1.63	1.42	0.88	1.74	1.52	1.54	1.36	1.61
$(La/Lu)_n$	7.64	8.37	10.06	10.78	13.39	18.91	12.44	17.82	9.93	3.49	2.88	4.07	3.84	3.77	3.78	15.19

* Analyses performed at Caltech.

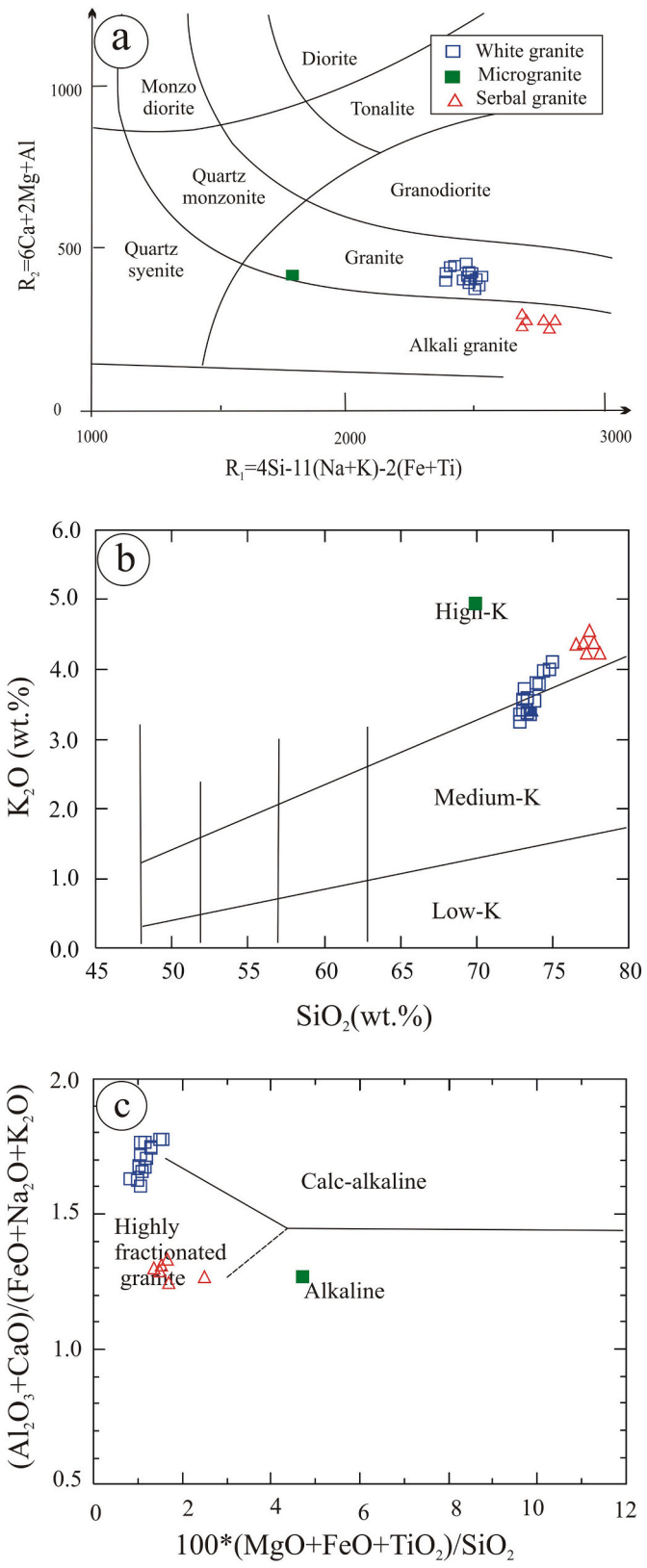

Fig. 7. Whole-rock geochemical characteristics of the UTP and associated granitoids: (a) petrological classification of the white granite of UTP using the R_1-R_2 diagram of De la Roche et al. (1980), (b) K_2O vs. SiO_2 classification diagram (Peccerillo and Taylor, 1976), and (c)$100*(MgO + FeO_{(t)} + TiO_2)/SiO_2$ vs. $(Al_2O_3 + CaO)/(FeO_{(t)} + Na_2O + K_2O)$ for distinguishing between calc-alkaline, highly fractionated calc-alkaline, and alkaline granites (Sylvester, 1989).

UTP granite samples range between 0.12 and 0.34 (average 0.21) (Table 3), which are similar to calc-alkaline granites of the Eastern Desert and Sinai (Rb/Sr < 1), whereas alkaline/peralkaline granites have Rb/Sr > 1 (Azer, 2006; Abdel-Rahman, 2006; Katzir et al., 2007; Khalil et al., 2018). Serbal pluton samples indeed have high Rb/Sr ratios (1.35–14.57, av. 8.75). The post-collisional setting for the UTP, the Serbal granite, and the microgranite is substantiated by plotting the geochemical data on the SiO_2-Al_2O_3 diagram of Maniar and Piccoli (1989) (Fig. 11a). Using the Y vs. Nb tectonic discrimination diagrams of Pearce et al. (1984), all the UTP samples plot in the field of volcanic-arc granite, whereas Serbal granite and microgranite plot in the within-plate field (Fig. 11b). On the Rb-Hf-Ta discrimination diagram of Harris et al. (1986), the analyzed samples of white granite plot in the late- to post-collision field (Fig. 11c).

Eyal et al. (2010) discussed the geology, geochemistry, and isotope data of post-collisional calc-alkaline and alkaline-peralkaline granites in the Sinai Peninsula (Egypt) and southern Israel. We compare the REE data for compiled 635–590 Ma plutonic rocks in the north ANS (Eyal et al., 2010) with the UTP, Serbal granite, and microgranite in Fig. 11d. It is evident that the UTP plots at the low-REE end of the regional post-collisional calc-alkaline group, whereas the Serbal pluton and microgranite plot within the field of alkaline granites of the ANS.

8.2. *Origin of the parental magma*

The post-collisional stage in the Sinai Peninsula was characterized by vast intrusions of calc-alkaline and alkaline/peralkaline granitoids and their associated volcanics. However, determining the origin of post-collisional calc-alkaline granitoids is complicated because they can be generated by a variety of processes and from various sources. There is no single petrogenetic model that satisfactorily explains the origin of all post-collisional calc-alkaline granites because they are the products of a complex set of processes. However, explanations that have been put forward generally fall into one of three groups: (1) extensive fractional crystallization from mantle-derived mafic magmas, (2) partial melting of various crustal sources, and (3) magma mixing between basaltic and crustal melts.

Generally, felsic rocks derived from fractional crystallization of mantle-derived magma should exhibit a continuous compositional trend from mafic through intermediate to felsic rocks (Kessel et al., 1998). The highly evolved nature of the UTP and the absence of any mafic or intermediate magmatic rocks of similar age and affinity argue against their formation from mantle-derived magma. On the other hand, granitoid magma comparable to the composition of the UTP can readily be produced through partial melting of a juvenile crustal source, possibly followed by some degree of fractional crystallization, upper crustal assimilation, filter pressing, or other shallow differentiation processes. The Neoproterozoic crustal basement rocks, which may represent potential magmatic sources, include gneisses, calc-alkaline granitoids (I-type), and calc-alkaline mafic rocks. Tonalitic gneisses are the most common rock type in the study area (El-Shafei and Kusky, 2003). On the ternary discrimination diagram of Laurent et al. (2014), the analyzed granite samples of UTP plot in the experimentally-calibrated field of melts derived from tonalite sources, suggesting that the UTP was indeed derived from a tonalitic source (Fig. 12). In fact, of the experimental data used by Laurent et al. (2014), the compositions that most resemble the composition of the UTP are from the fluid-absent melting experiments on a high-Na amphibole-bearing tonalite generated by Watkins et al. (2007); other studies have yielded liquids too low in Na_2O.

The experimental melts produced directly from high-Na tonalite sources are similar to the observed rocks, without any need for hidden fractional crystallization or assimilation processes at stages of evolution more primitive than those directly sampled by the intrusion. This is consistent with the small and unsystematic Eu anomalies observed in the UTP, since extensive feldspar fractionation would generate systematically negative Eu anomalies. Instead, the anomalies in the trace element

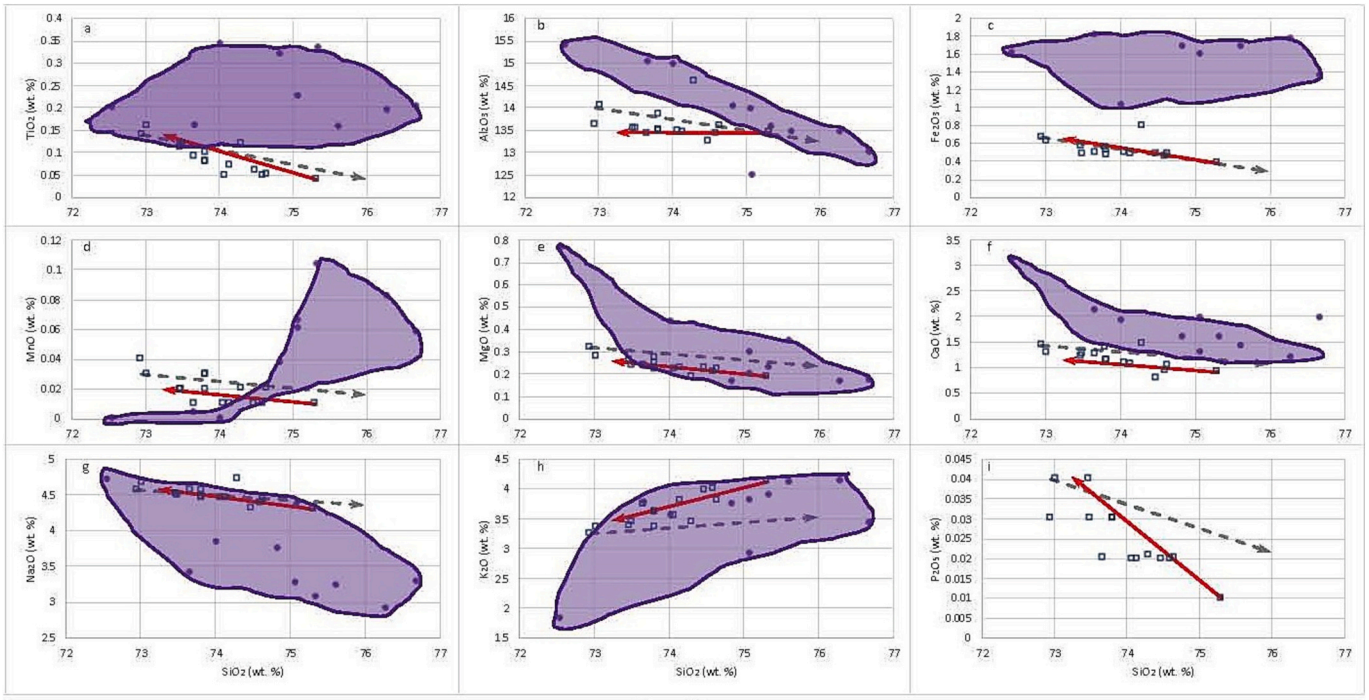

Fig. 8. Variation diagrams of some major oxides against SiO_2 for the Um Takha Pluton white granite. The dashed arrows show a best-fitting liquid-line-of-descent fractional crystallization model, whereas the solid arrows show a best-fitting variable-proportion cumulate-liquid sampling model. The shaded fields and solid circles show the glass compositions from the vapor-absent Na-rich amphibole tonalite melting experiments of Watkins et al. (2007).

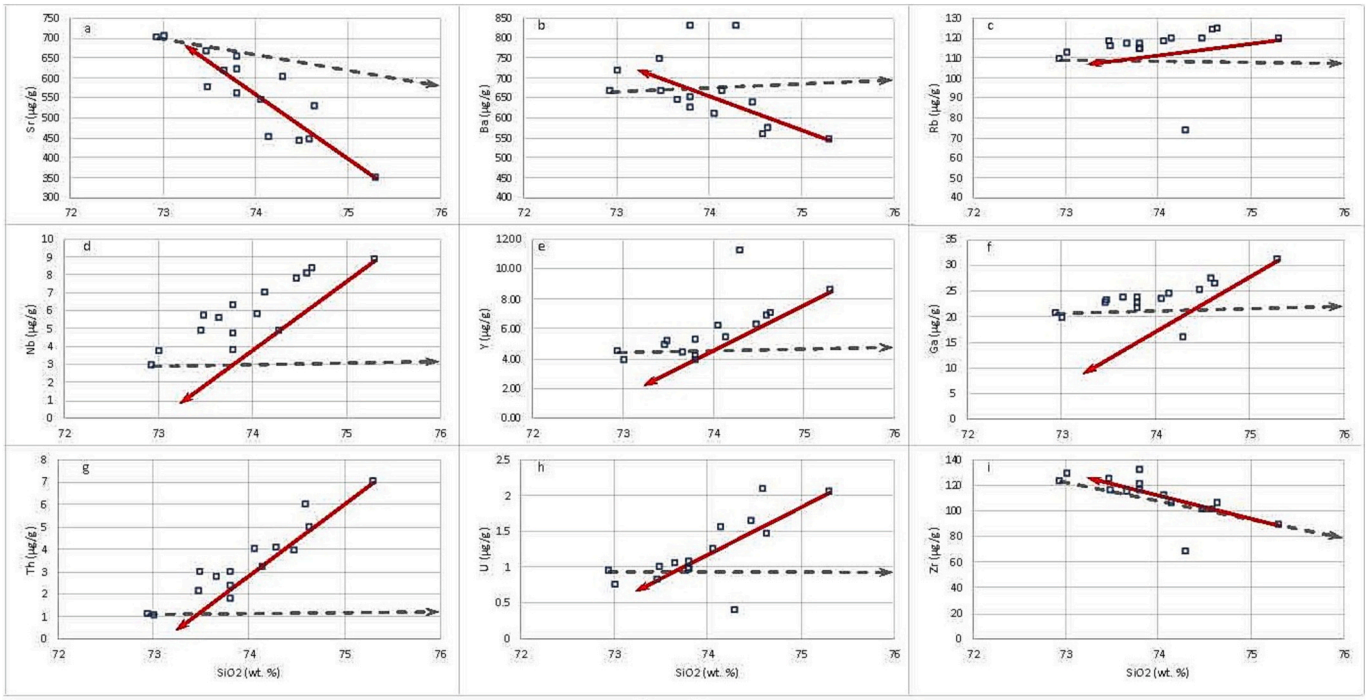

Fig. 9. Variation diagrams of some trace elements against SiO_2 for the Um Takha Pluton white granite. The dashed arrows show a best-fitting liquid-line-of-descent fractional crystallization model, whereas the solid arrows show a best-fitting variable-proportion cumulate-liquid sampling model.

patterns of the UTP samples may be explained in terms of the residual mineralogy of the melting source. The very low concentration of rare earth elements (37–67 µg/g) implies residual REE-rich phases (like zircon, monazite, allanite, xenotime, apatite and possibly garnet) that were not exhausted from the source (Gelman et al., 2014; Li and Huang, 2013). Likewise, the concave-up HREE pattern in the UTP (Fig. 10b) suggests equilibration with residual amphibole and the moderate Eu anomalies in UTP samples do imply various roles for feldspar in the melting regime, along their ascent, or in the magma chamber (Wu et al., 2017). Low Ti and P in the UTP suggest residual ilmenite and apatite. All the necessary residual major phases (amphibole, feldspar, and ilmenite) were observed experimentally by Watkins et al. (2007). We note that a

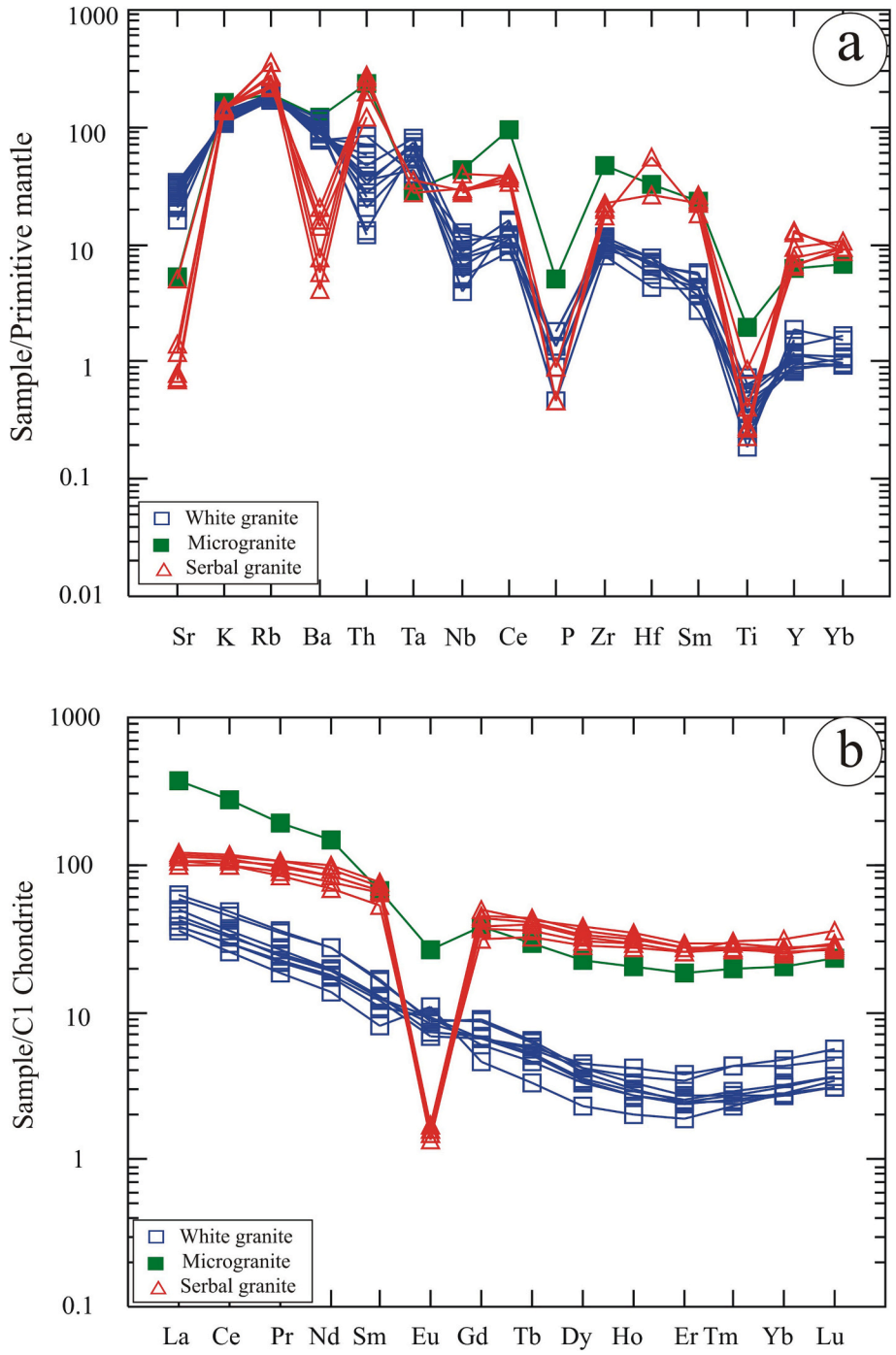

Fig. 10. (a) Primitive mantle normalized multi-element diagrams for the UTP white granite, Serbal granite and microgranite; normalization values from Sun and McDonough (1989). (b) Chondrite-normalized REE patterns for the white granite, Serbal granite and microgranite; chondrite values from Evensen et al. (1978).

primary melt model with trace element fractionations controlled by residual assemblages would not, by contrast, work for the Serbal alkaline granite, with its nearly two order-of-magnitude negative Eu, Sr, and Ba anomalies.

Thermal and tectonic models that explain the post-collisional melting of the ANS crust generally require elevation of the crustal geotherm due to underplating of mantle-derived basaltic magma (Litvinovsky et al., 2021). But this mantle-derived component may only be a source of heat and not of mass for the crustal magmatic system. Many authors have hoped to resolve the relative role of mantle-derived and crustal sources for the post-collisional magmas of the ANS using radiogenic isotope data. In general, the upper mantle was depleted by the extraction of continental crust, leaving superchondritic Sm/Nd and Lu/Hf ratios in the residue, leading over time to positive values of ε_{Nd} and ε_{Hf} relative to a chondritic reference. On the other hand, crustal rocks form from melts that are more enriched in more incompatible elements and so have low Sm/Nd and Lu/Hf ratios that drive evolution, over time, towards negative values of ε_{Nd} and ε_{Hf}. The difficulty in the ANS case is that the lower crust during the post-collision period (ca. 620–590 Ma) was extremely juvenile at that time, having formed during the immediately preceding collisional stage (as young, in some cases, as 635 Ma). Tonalitic mafic rocks in the lower crust are not extraordinarily enriched and their isotope ratios evolve slowly. There was not time for the juvenile ANS lower crust to evolve to negative ε_{Hf} before being remelted in

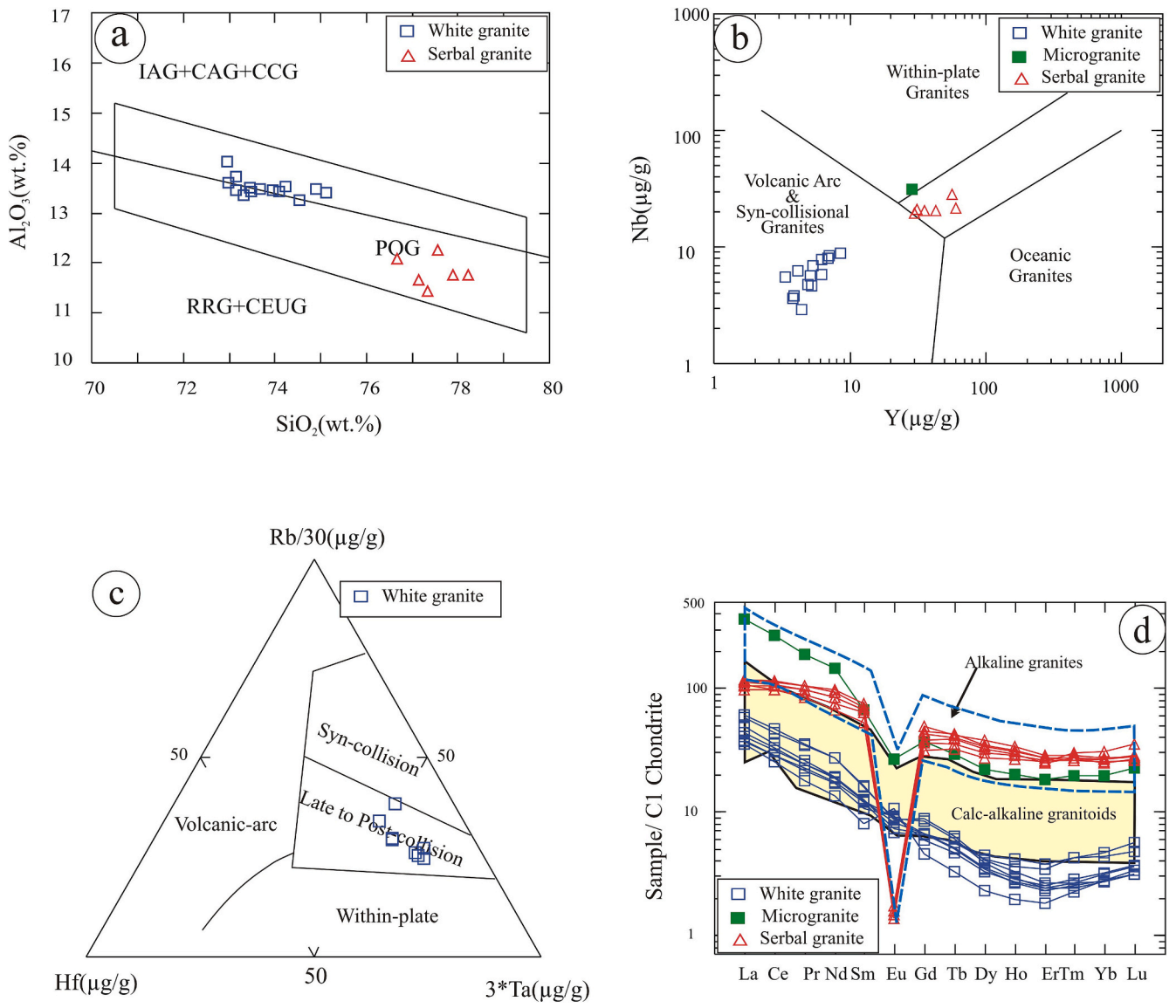

Fig. 11. Diagrams for classifying the geotectonic affinity of the UTP and associated granitoids: (a) SiO_2 vs. Al_2O_3 diagram (Maniar and Piccoli, 1989), (b) Y vs. Nb tectonic discrimination diagram (Pearce et al., 1984), (c) Hf-Rb/30–3*Ta ternary diagram (Harris et al., 1986), and (d) comparison of chondrite-normalized REE patterns to fields of typical calc-alkaline and alkaline granitoid suites in the ANS (Azer, 2013).

the post-collisional stage. For this reason, isotopic studies have not yielded a definitive resolution of the debate about the relative role of mantle and crustal sources for these rocks. The present zircon Hf isotope results are entirely consistent with results from similar post-collisional calk-alkaline granitoids throughout the ANS (Johnson, 2014). Although present day $\varepsilon_{Hf}(0)$ values are consistently negative, reflecting 615 Ma of evolution in a crustal setting, extrapolation back to the magmatic age yields uniformly positive $\varepsilon_{Hf}(t)$ values, about +5 to +7. These values do not distinguish between (a) direct derivation of the parental magma by asthenospheric melting at the time of delamination and (b) a short period of storage of the source material as tonalitic rocks in the lower crust before remelting in response to a delamination-driven heat pulse. The other criteria discussed above continue to favor the latter hypothesis.

Many authors have linked basaltic underplating to lithospheric delamination as a driver for post-collisional (620–590 Ma) magmatism in the ANS (Abdallah et al., 2020; Farahat and Azer, 2011). The emplacement of the UTP was associated with extensive denudation of the pre-630 Ma orogenic edifice as well as the 630–600 Ma post-collisional products. Such a scenario implies thinning of the previously thickened lithosphere, facilitating the upwelling of hot asthenospheric material, crustal doming, and extension (e.g., Avigad and Gvirtzman, 2009). The generation of crustal melts by lithospheric delamination was likely facilitated by a combination of elevation of the crustal geotherm (due to input of mantle-derived heat) and exhumation of the deep crust to low pressure (due to erosion of overburden resulting from uplift). According to Avigad and Gvirtzman (2009), lithospheric removal results in upwelling of hot asthenosphere and crustal uplift, up to ~3 km in the northern ANS. Through the lithospheric delamination process, upwelling hot asthenosphere generated mafic magma that underplated the lower crust to promote its partial melting and to generate the late-collisional calc-alkaline granitoids. Ascent of the resulting melts to the middle and upper crust was in turn likely facilitated by the large-scale intra-continental strike-slip fault systems and shear zones that established a transtensional to local extensional tectonic environment. This large-scale melting could account for the wide area distribution of post-collisional magmatism in the northern ANS (Farahat and Azer, 2011).

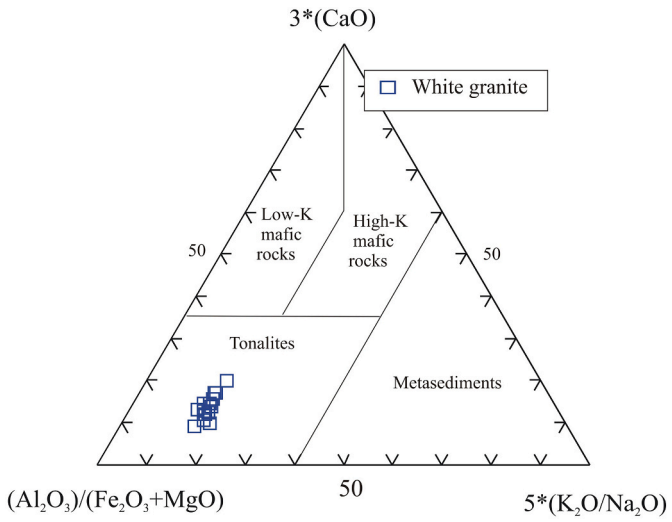

Fig. 12. $Al_2O_3/(Fe_2O_3 + MgO)$-3CaO-5(K_2O/Na_2O) petrogenetic discrimination diagram for the UTP white granite (Laurent et al., 2014).

8.3. *Fractional crystallization vs. variable-proportion liquid-cumulate sampling*

Igneous petrologists are trained to presume that suites of related magmatic rocks, excepting those with obvious cumulate textures, are related to one another by fractional crystallization along a liquid line of descent (Grove and Brown, 2018). However, plutonic rocks are evidently made of crystals, not liquid. Considering the high viscosity of granitoid magma, which suppresses crystal fractionation, it is not axiomatic that a suite of related plutonic rocks should in fact represent a liquid line of descent. In the UTP, in particular, some compositional trends appear consistent with fractional crystallization but it is not possible to simultaneously explain the major and trace element variation across the suite using a single liquid line of descent model.

The impossibility of modeling all the UTP data as a liquid line of descent is perhaps most easily seen by considering the mass of solids that must be fractionated from a liquid equivalent to the lowest-SiO_2 sample to evolve it to a residual liquid equivalent to the highest-SiO_2 sample. A successful model must simultaneously explain the major and trace element trends. A simple mass balance calculation shows that the best-fitting fractionating assemblage — explaining the slopes of the suite in plots of TiO_2, Al_2O_3, Fe_2O_3, MnO, MgO, CaO, Na_2O, K_2O, and P_2O_5 against SiO_2 — is 15% biotite (with Mg# 35), 1% ilmenite, 0.35% apatite, 0.03% zircon, and the remainder oligoclase ($Ab_{73}An_{27}Or_0$) (this fractionation trend is shown in Fig. 8 and the phase proportions and compositions are given in Supplementary Table S6). Removal of just 10% by mass of this assemblage spans the entire major element range of the sampled suite of UTP rocks. The only way to fractionate more mass while spanning this range would involve a higher-SiO_2 solid fractionating assemblage, but the increase in K_2O with SiO_2 shows that alkali feldspar is not a major fractionating phase and rhyoliteMELTS (Gualda et al., 2012) calculations show that quartz saturation is not achieved except at the highest-SiO_2 end of the trend. Hence 10% mass fractionation is a robust estimate. However, across the same sample suite, the dynamic range of trace element concentration changes is quite large: Sr decreases by a factor of 2.5, while the HREEs increase by 40–60%, Y increases by a factor of 1.9, Nb increases by a factor of 3, and Th increases by a factor of 6.3. It is no problem, in principle, for elements compatible in the fractionating assemblage to decrease sharply during fractional crystallization, though it would require an unreasonably high partition coefficient of Sr into oligoclase (about 6). The incompatible elements, however, show that the liquid line of descent model fails completely. The extreme case that the HREEs, Y, Nb, and Th were acting perfectly incompatibly during fractionation provides an upper bound on the amount by which their concentrations can increase in the residual liquid, equal to the mass fraction of solids removed, specifically 10%. The failure of the fractionation model to explain the trace element trends

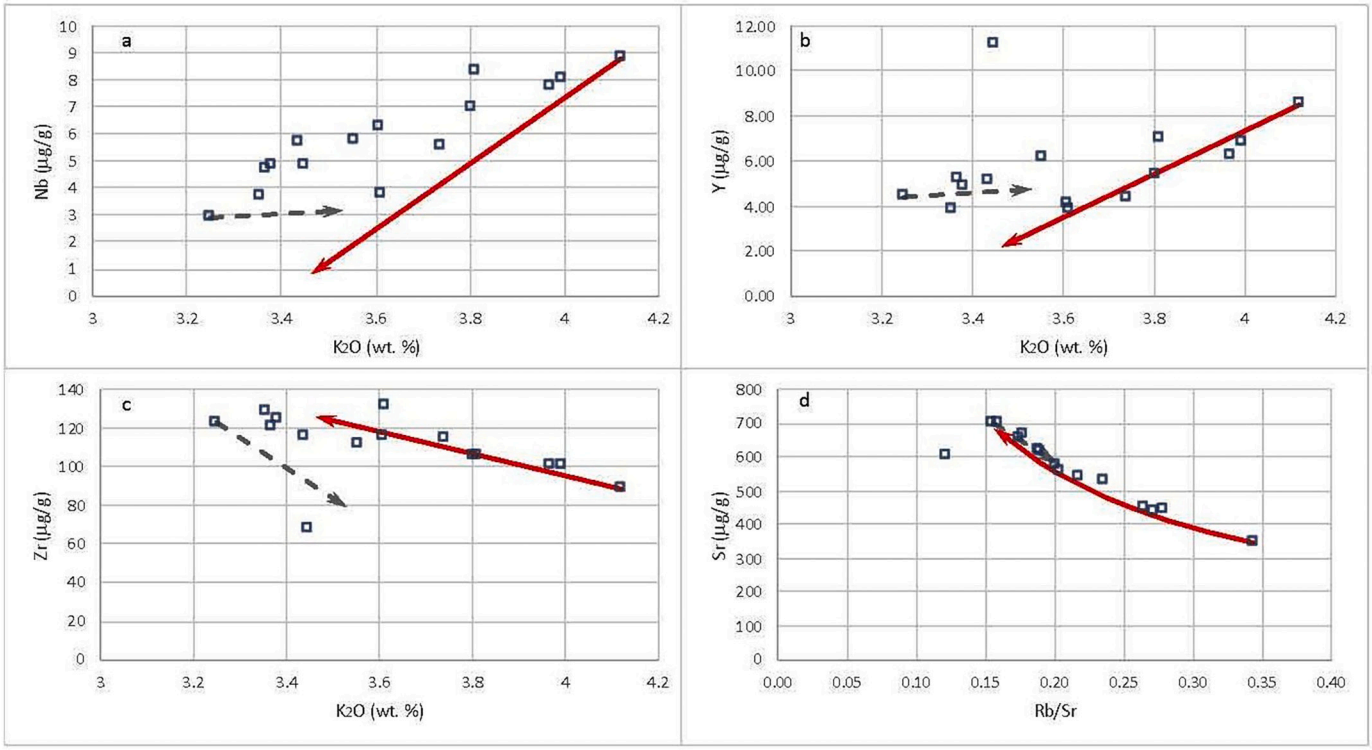

Fig. 13. Bivariate diagrams comparing the UTP white granite samples to predictions of a liquid-line-of-descent fractional crystallization differentiation trend (dashed arrows) and a variable-proportion liquid-cumulate sampling model (solid arrows): (a) K_2O vs. Nb, (b) K_2O vs. Y, (c) K_2Ovs. Zr, and (d) Rb/Sr vs. Sr.

is shown in Fig. 9 and Fig. 13.

The failure of fractional crystallization to simultaneously explain the major and trace element variations across the UTP suite motivates a search for alternative models. One class of models is assimilation/fractional crystallization (AFC) models, which suppose that some upper crustal component (e.g., a partial melt of the country rock) is added to the magma as it evolves. Indeed, the presence of gneissose diorite xenoliths in the UTP suggests some mingling and thus possible mixing of foreign material into the magma. However, such models are unlikely to succeed in explaining the trace element systematics, because the country rock is much more depleted than the UTP (granodiorite and diorite), having a higher melting point and lower concentrations of trace elements. An assimilation model also has difficulty explaining a factor of 2.5 decrease in Sr concentration.

Instead, we suggest that the rock compositions of the UTP are best viewed as a series from a pure liquid composition (at the high-SiO_2 end) to a crystal-liquid mixture or mush (at the low-SiO_2 end). In principle, the low-SiO_2 end member could be a pure cumulate with no residual liquid, as an extreme case, but then it would likely have even lower trace element contents. A variable-proportion crystal-liquid sampling model more easily explains significant variations in the ratios of more-or-less equally incompatible elements — such as K/Rb, Zr/Rb and Ba/Nb (Table 3) —than a simple fractional crystallization model (Davidson et al., 1987). We find a reasonably successful model in which various proportions from 6% to 100% of the most evolved liquid (sample M3b) are mixed with an assemblage of solids similar to the CIPW norm of the least evolved sample (M15) — 41% oligoclase ($Ab_{85}An_{15}$), 31% quartz, 20% orthoclase, 1.6% biotite (with Mg# 35), 0.2% magnetite, 0.17% ilmenite (with 5 wt% MnO), 0.07% apatite, and 0.01% zircon. All of the solids are assumed to be in equilibrium with the liquid, using partition coefficients selected from the TraceDs database (https://lepr.earthchem.org) and shown in Supplementary Table 6S. This reasonably successful variable-proportion crystal-liquid sampling model is shown in Fig. 8 (for major elements), Fig. 9 (for trace elements against SiO_2), and Fig. 13 (for selected trace element ratios).

Finding a paradigm less limiting than liquid line of descent modeling for explaining whole-rock compositional variations within granitoid plutons has been a notable goal in igneous petrology for decades (Grove and Brown, 2018). The UTP case offers a simple case where one such alternative model, a spectrum from a liquid composition to a nearly pure cumulate of solids in equilibrium with that liquid, appears to work well.

9. Conclusions

- The Um Takha Pluton consists of a single co-genetic suite of undeformed, post-collisional white granites of mostly high-K calc-alkaline affinity. It intrudes metasediments, granodiorite, and diorite of the subduction stage of the Arabian-Nubian Shield and is, in-turn, intruded by the alkaline Serbal pluton and a small mass of microgranite.
- The crystallization age of the Um Takha Pluton is most likely 614.9 ± 6.3 Ma, based on a cluster of three overlapping nearly concordant U-Pb ages in one sample. However, other zircons in this sample and nearly all zircons in another sample are disturbed. This age is consistent with the intrusive relations observed locally and with the time period of post-collisional calc-alkaline magmatism in the northernmost Arabian-Nubian Shield.
- The Hf isotope ratios in the dated zircons yield positive calculated values of $\varepsilon_{Hf}(614.9)$ that are consistent with derivation from juvenile crustal materials stored for a short time in the lower crust of the ANS.
- The Um Takha Pluton is most likely derived by partial melting of a high-Na amphibole-bearing tonalite from the juvenile crust of the Arabian-Nubian Shield, likely triggered by the thermal disturbance associated with lithosphere delamination.
- The compositional range observed among samples of the white granite, limited in major elements but quite large in some trace elements, is difficult to reconcile with classical fractional crystallization scenario but can be modeled as a variation from a magmatic liquid composition to a low-melt fraction cumulate mush.

Declaration of Competing Interest

The authors declare that they have no known competing financial interests or personal relationships that could have appeared to influence the work reported in this paper.

Acknowledgements

The authors would like to extend their appreciation and gratitude to the editor (Greg Shellnutt) and two anonymous reviewers for their efforts and numerous helpful comments. The Arizona LaserChron Center is supported by NSF awards EAR-2050246 and 2153415. PDA is supported by NSF award EAR-1947616. This paper is dedicated to the memory of Maxiar (Max) H. Wang, whose work was essential to the geochronological study. We thank Ming-Chang Liu and Elizabeth Bell for support in the UCLA National Ion Probe facility

Appendix A. Supplementary data

Supplementary data to this article can be found online at https://doi.org/10.1016/j.lithos.2023.107021.

References

Abdallah, S.E., Azer, M.K., El Shammari, A.S., 2020. Petrological and geochemical evolution of Ediacaran rare-metal bearing A-type granites from Jabal Aja complex, northern Arabian Shield, Saudi Arabia. Acta Geol. Sin. 94 (3), 743–762.
Abdel-Rahman, A.M., 1994. Nature of biotites from alkaline, calc-alkaline and peraluminous magmas. J. Petrol. 35, 525–541.
Abdel-Rahman, A.M., 2006. Petrogenesis of anorogenic peralkaline granitic complexes from eastern Egypt. Mineral. Mag. 70, 27–50.
Abuamarah, B.A., Azer, M.K., Asimow, P.D., Shi, Q., 2021a. Post-collisional volcanism with adakitic signatures in the Arabian-Nubian Shield: a case study of calc-alkaline Dokhan volcanics in the Eastern Desert of Egypt. Lithos 388, 106051.
Abuamarah, B.A., Azer, M.K., Mubarak, H.S., 2021b. Origin and magmatic evolution of late Neoproterozoic post-accretion high-K calc-alkaline adakitic volcanics in the northern Arabian–Nubian Shield. Am. J. Sci. 321 (5), 534–578.
Abuamarah, B.A., Azer, M.K., Seddik, A.M., Asimow, P.D., Guzman, P., Fultz, B.T., Wilner, M.J., Dalleska, N., Darwish, M.H., 2022. Magmatic and post-magmatic evolution of post-collisional rare-metal bearing granite: the Neoproterozoic Homrit Akarem Granitic Intrusion, south Eastern Desert of Egypt, Arabian-Nubian Shield. Geochemistry 82 (1), 125840.
Ali, K.A., Azer, M.K., Gahlan, H.A., Wilde, S.A., Samuel, M.D., Stern, R.J., 2010. Age constraints on the formation and emplacement of Neoproterozoic ophiolites along the Allaqi Suture, south Eastern Desert, Egypt. Gondwana Res. 18, 583–595.
Avigad, D., Gvirtzman, Z., 2009. Late Neoproterozoic rise and fall of the northern Arabian–Nubian Shield: the role of lithospheric mantle delamination and subsequent thermal subsidence. Tectonophysics 477 (3–4), 217–228.
Azer, M.K., 2006. The petrogenesis of late Precambrian felsic alkaline magmatism in South Sinai, Egypt. Acta Geol. Pol. 56 (4), 463–484.
Azer, M.K., 2007. Tectonic significance of Late Precambrian calc-alkaline and alkaline magmatism in Saint Katherina area, southern Sinai, Egypt. Geologica Acta: an international earth science journal 5 (3), 255–272.
Azer, M.K., 2013. Late Ediacaran (605–580 Ma) post-collisional alkaline magmatism in the Arabian–Nubian Shield: a case study of Serbal ring-shaped intrusion, southern Sinai, Egypt. J. Asian Earth Sci. 77, 203–223.
Azer, M.K., Asimow, P.D., 2021. Petrogenetic evolution of the Neoproterozoic igneous rocks of Egypt. In: The Geology of the Egyptian Nubian Shield. Springer, Cham, pp. 343–382.
Azer, M.K., El-Ela, F.A., Ren, M., 2012. The petrogenesis of late Neoproterozoic mafic dyke-like intrusion in south Sinai, Egypt. J. Asian Earth Sci. 54, 91–109.
Azer, M.K., Farahat, E.S., 2011. Late Neoproterozoic volcano-sedimentary succession of Wadi Rufaiyil, southern Sinai, Egypt: a case of transition from late- to post-collisional magmatism. J. Asian Earth Sci. 42, 1187–1203.
Azer, M.K., Stern, R.J., Kimura, J.-I., 2010. Origin of a late Neoproterozoic (605±13 Ma) intrusive carbonate-albitite complex in Southern Sinai, Egypt. Int. J. Earth Sci. 99, 245–267.
Azer, M.K., Gahlan, H.A., Asimow, P.D., Al-Kahtany, K.M., 2017. The late Neoproterozoic Dahanib mafic-ultramafic intrusion, South eastern Desert, Egypt: Is it an Alaskan-type or a layered intrusion? Am. J. Sci. 317 (8), 901–940.
Azer, M.K., Gahlan, H.A., Asimow, P.D., Mubarak, H.S., Al-Kahtany, K.M., 2019. Multiple stages of carbonation and element redistribution during formation of ultramafic-

hosted magnesite in Neoproterozoic ophiolites of the Arabian-Nubian Shield, Egypt. The J. Geol. 127 (1), 81–107.
Azer, M.K., Obeid, M.A., Ren, M., 2014. Geochemistry and petrogenesis of late Ediacaran (605–580 Ma) post-collisional alkaline rocks from the Katherina ring complex, South Sinai, Egypt. J. Asian Earth Sci. 93, 229–252.
Be'eri-Shlevin, Y., Katzir, Y., Valley, J.W., 2009a. Crustal evolution and recycling in a juvenile continent: Oxygen isotope ratio of zircon in the northern Arabian Nubian Shield. Lithos 107, 169–184.
Be'eri-Shlevin, Y., Katzir, Y., Whitehouse, M., 2009b. Post-collisional tectonomagmatic evolution in the northern Arabian–Nubian Shield: time constraints from ion-probe U–Pb dating of zircon. J. Geol. Soc. 166 (1), 71–85.
Be'eri-Shlevin, Y., Samuel, M.D., Azer, M.K., Rämö, O.T., Whitehouse, M.J., Moussa, H. E., 2011. The Ediacaran Ferani and Rutig volcano-sedimentary successions of the northernmost Arabian-Nubian Shield (ANS): new insights from zircon U–Pb geochronology, geochemistry and O–Nd isotope ratios. Precambrian Res. 188 (1–4), 21–44.
Black, L.P., Kamo, S.L., Allen, C.M., Davis, D.W., Aleinikoff, J.N., Valley, J.W., Mundil, R., Campbell, I.H., Korsch, R.J., Williams, I.S., Foudoulis, C., 2004. Improved 206Pb/238U microprobe geochronology by the monitoring of a trace-element-related matrix effect; SHRIMP, ID–TIMS, ELA–ICP–MS and oxygen isotope documentation for a series of zircon standards. Chem. Geol. 205 (1–2), 115–140.
Davidson, J.P., Dungan, M.A., Ferguson, K.M., Colucci, M.T., 1987. Crust-magma interactions and the evolution of arc magmas: The San Pedro–Pellado volcanic complex, southern Chilean Andes. Geology 15 (5), 443–446.
De la Roche, H., Leterrier, J., Grandclaude, P., Marchal, M., 1980. A classification of volcanic and plutonic rocks using R_1-R_2 diagrams and major-element analyses — its relationship with current nomenclature. Chem. Geol. 29, 183–210.
Deer, W.A., Howie, R.A., Zussman, J., 1992. An Introduction to the Rock Forming Minerals, Second edition. Longman Scientific and Technical, London, p. 696.
Eddy, M.P., Jagoutz, O., Ibañez-Mejia, M., 2017. Timing of initial seafloor spreading in the Newfoundland-Iberia rift. Geology G38766, 1–22.
El-Shafei, M.K., Kusky, T.M., 2003. Structural and tectonic evolution of the Neoproterozoic Feiran–Solaf metamorphic belt, Sinai Peninsula: implications for the closure of the Mozambique Ocean. Precambrian Res. 123, 269–293.
Evensen, N.M., Hamilton, P.J., O'Nions, R.K., 1978. Rare earth abundances in chondritic meteorites. Geochim. Cosmochim. Acta 42 (8), 1199–1212.
Eyal, M., Litvinovsky, B., Jahn, B.M., Zanvilevich, A., Katzir, Y., 2010. Origin and evolution of post-collisional magmatism: coeval Neoproterozoic calc-alkaline and alkaline suites of the Sinai Peninsula. Chem. Geol. 269 (3–4), 153–179.
Eyal, M., Be'eri-Shlevin, Y., Eyal, Y., Whitehouse, M.J., Litvinovsky, B., 2014. Three successive Proterozoic island arcs in the Northern Arabian–Nubian Shield: Evidence from SIMS U–Pb dating of zircon. Gondwana Res. 25 (1), 338–357.
Eyal, M., Bentor, Y.K., Shimron, A.E., Eyal, Y., Calvo, R., Hall, J.K., 2015. Geological map of Feiran Metamorphic Belt, SinaiEgypt, Scale 1:75000. Geological Survey of Israel.
Farahat, E.S., Azer, M.K., 2011. Post-collisional magmatism in the northern Arabian–Nubian Shield: the geotectonic evolution of the alkaline suite at G. Tarbush area, south Sinai, Egypt. Chem. Erde 71, 247–266.
Frei, D., Gerdes, A., 2009. Precise and accurate in situ U–Pb dating of zircon with high sample throughput by automated LA-SF-ICP-MS. Chem. Geol. 261 (3–4), 261–270.
Gahlan, H.A., Azer, M.K., Asimow, P.D., Al-Kahtany, K.M., 2016. Late Ediacaran post-collisional A-type syenites with shoshonitic affinities, northern Arabian-Nubian Shield: a possible mantle-derived A-type magma. Arab. J. Geosci. 9 (12), 1–24.
Gelman, S.E., Deering, C.D., Bachmann, O., Huber, C., Gutierrez, F.J., 2014. Identifying the crystal graveyards remaining after large silicic eruptions. Earth Planet. Sci. Lett. 403, 299–306.
Gion, A.M., Piccoli, P.M., Candela, P.A., 2022. Characterization of biotite and amphibole compositions in granites. Contrib. Mineral. Petrol. 177 (4), 1–15.
Grove, T.L., Brown, S.M., 2018. Magmatic processes leading to compositional diversity in igneous rocks: Bowen (1928) revisited. Am. J. Sci. 318 (1), 1–28.
Gualda, G.A.R., Ghiorso, M.S., Lemons, R.V., Carley, T.L., 2012. Rhyolite-MELTS: a modified calibration of MELTS optimized for silica-rich, fluid-bearing magmatic systems. J. Petrol. 53 (5), 875–890.
Harris, N.B., Pearce, J.A., Tindle, A.G., 1986. Geochemical characteristics of collision-zone magmatism. In: Coward, M.P., Ries, A.C. (Eds.), Collision Tectonics, Journal of Geological Society, London, Special Publication, vol. 19, pp. 67–81.
Hussein, A.A.A., Ali, M.M., El Ramly, M.F., 1982. A proposed new classification of the granites of Egypt. J. Volcanol. Geotherm. Res. 14 (1–2), 187–198.
Ibañez-Mejia, M., Gehrels, G.E., Ruiz, J., Vervoort, J.D., Eddy, M.P., Li, C., 2014. Small-volume baddeleyite (ZrO2) U–Pb geochronology and Lu–Hf isotope geochemistry by LA-ICP-MS. Techniques and applications. Chem. Geol. 384, 149–167.
Ibañez-Mejia, M., Pullen, A., Arenstein, J., Gehrels, G.E., Valley, J., Ducea, M.N., Mora, A.R., Pecha, M., Ruiz, J., 2015. Unraveling crustal growth and reworking processes in complex zircons from orogenic lower-crust: the Proterozoic Putumayo Orogen of Amazonia. Precambrian Res. 267, 285–310.
Johnson, P.R., 2003. Post-amalgamation basins of the NE Arabian shield and implications for Neoproterozoic III tectonism in the northern East African orogen. Precambrian Res. 123, 321–338.
Johnson, P.R., 2014. An expanding Arabian-Nubian Shield geochronologic and isotopic dataset: defining limits and confirming the tectonic setting of a Neoproterozoic accretionary orogen. The Open Geol. J. 8 (1), 3–33.
Katzir, Y., Eyal, M., Litvinovsky, B.A., Jahn, B.M., Zanvilevich, A.N., Valley, J.W., Beeri, Y., Pelly, I., Shimshilashvili, E., 2007. Petrogenesis of A-type granites and origin of vertical zoning in the Katharina pluton, Gebel Mussa (Mt. Moses) area, Sinai, Egypt. Lithos 95 (3–4), 208–228.
Kessel, R., Stein, M., Navon, O., 1998. Petrogenesis of Late Neoproterozoic dikes in the Northern Arabian–Nubian Shield: implications for the origin of A-type granites. Precamb. Res. 92 (2), 195–213.
Khalil, A.E.S., Obeid, M.A., Azer, M.K., Asimow, P.D., 2018. Geochemistry and petrogenesis of post-collisional alkaline and peralkaline granites of the Arabian-Nubian Shield: a case study from the southern tip of Sinai Peninsula, Egypt. Int. Geol. Rev. 60 (8), 998–1018.
Laurent, O., Martin, H., Moyen, J.F., Doucelance, R., 2014. The diversity and evolution of late-Archean granitoids: evidence for the onset of "modern-style" plate tectonics between 3.0 and 2.5 Ga. Lithos 205, 208–235.
Li, J., Huang, X.L., 2013. Mechanism of Ta-Nb enrichment and magmatic evolution in the Yashan granites, Jiangxi Province, South China (in Chinese). Acta Petrol. Sin. 29, 4311–4322.
Liégeois, J.P., Black, R., 1987. Alkaline magmatism subsequent to collision in the Pan-African belt of the Adrar des Iforas. In: Fitton, J.G., Upton, B.G.J. (Eds.), Alkaline Igneous Rocks, Geological Society, Special Publication, vol. 30, pp. 381–401.
Liégeois, J.P., Navez, J., Black, R., Hertogen, J., 1998. Contrasting origin of post-collision high-K calc-alkaline and shoshonitic versus alkaline and peralkaline granitoids, The use of sliding normalization. Lithos 45, 1–28.
Litvinovsky, B.A., Vapnik, Y., Eyal, M., Eyal, Y., 2021. The role of mantle and the ancient continental crust in the generation of post-collisional high-K calc-alkaline and alkaline granites, with main reference to the Arabian-Nubian Shield. Lithos 388, 106049.
Maniar, P.D., Piccoli, P.M., 1989. Tectonic discrimination of granitoids. Geol. Soc. Am. Bull. 101 (5), 635–643.
Meert, J.G., 2003. A synopsis of events related to the assembly of eastern Gondwana. Tectonophysics 362, 1–40.
Moreno, J.A., Montero, P., Abu Anbar, M., Molina, J.F., Scarrow, J.H., Talavera, C., Cambeses, A., Bea, F., 2012. SHRIMP U-Pb zircon dating of the Katerina Ring complex: Insights into the temporal sequence of Ediacaran calc-alkaline to peralkaline magmatism in southern Sinai, Egypt. Gondwana Res. 12, 887–900.
Nachit, H., 1985. Composition chemique des biotites et typologie magmatique des granitoids. Comtes Rendus Hebdomadaires de l'Academie des Sciences 301 (11), 813–818.
Nachit, H., Ibhi, A., Abia, E.H., Ohoud, M.B., 2005. Discrimination between primary magmatic biotites, reequilibrated biotites and neoformed biotites. Comptes Rendus Géoscience 337, 1415–1420.
Paces, J.B., Miller Jr, J.D., 1993. Precise U-Pb ages of Duluth complex and related mafic intrusions, northeastern Minnesota: geochronological insights to physical, petrogenetic, paleomagnetic, and tectonomagmatic processes associated with the 1.1 Ga midcontinent rift system. J. Geophys. Res. Solid Earth 98 (B8), 13997–14013.
Patchett, P.J., Chase, C.G., 2002. Role of transform continental margins in major crustal growth episodes. Geology 30, 39–42.
Patchett, P., Tatsumoto, M., 1980. Hafnium isotope variations in oceanic basalts. Geophys. Res. Lett. 7, 1077–1080.
Pearce, J.A., Harris, N.B.W., Tindle, A.G., 1984. Trace element discrimination diagrams for the tectonic interpretation of granitic rocks. J. Petrol. 25, 956–983.
Peccerillo, A., Taylor, S.R., 1976. Geochemistry of Eocene calc-alkaline volcanic rocks from the Kastamonu area, northern Turkey. Contrib. Mineral. Petrol. 58 (1), 63–81.
Schmitz, Mark D., Samuel, A. Bowring, Trevor, R. Ireland, 2003. Evaluation of Duluth Complex anorthositic series (AS3) zircon as a U-Pb geochronological standard: New high-precision isotope dilution thermal ionization mass spectrometry results. Geochim. et Cosmochim. Acta 67 (19), 3665–3672.
Sisson, T.W., 1994. Hornblende-melt trace-element partitioning by ion microprobe. Chem. Geol. 117, 331–344.
Stern, R.J., Johnson, P.J., Kröner, A., Yibas, B., 2004. Neoproterozoic ophiolites of the Arabian–Nubian Shield. In: Kusky, T. (Ed.), Precambrian Ophiolites. Elsevier, pp. 95–128.
Stoeser, D.B., Frost, C.D., 2006. Nd, Pb, Sr, and O isotopic characterization of Saudi Arabian Shield terranes. Chem. Geol. 226, 163–188.
Störmer, J.C., 1983. The effects of recalculation on estimates of temperature and oxygen fugacity from analyses of multicomponent iron-titanium oxides. Am. Mineral. 68 (5–6), 586–594.
Sun, S., McDonough, W.F., 1989. Chemical and isotopic systematic of oceanic basalts: implications for mantle compositions and processes. Magmatism in the Ocean Basins. In: Saunders, A.D., Norry, M.J. (Eds.), Geological Society of London, Special Publication, 42, pp. 313–345.
Sylvester, P.J., 1989. Post-collisional alkaline granites. J. Geol. 97 (3), 261–280.
Vervoort, J., Patchett, P., Söderlund, U., Baker, M., 2004. Isotopic composition of Yb and the determination of Lu concentrations and Lu/Hf ratios by isotope dilution using MC-ICPMS. Geochem. Geophys. Geosyst. 5, Q11002.
Watkins, J.M., Clemens, J.D., 2007. Archaean TTGs as sources of younger granitic magmas: melting of sodic metatonalites at 0.6–1.2 GPa. Contrib. Mineral. Petrol. 154 (1), 91–110.
Watkins, J.M., Clemens, J.D., Treloar, P.J., 2007. Archaean TTGs as sources of younger granitic magmas: melting of sodic metatonalites at 0.6–1.2 GPa. Contrib. Mineral. Petrol. 154, 91–110.
Woodhead, J.D., Hergt, J.M., 2005. A preliminary Appraisal of seven Natural Zircon Reference Materials for in Situ Hf Isotope Determination. Geostand. Geoanal. Res. 29, 183–195.
Wu, F., Liu, X., Ji, W., Wang, J., Yang, L., 2017. Highly fractionated granites: Recognition and research. Sci. China Earth Sci. 60 (7), 1201–1219.